NOVA SCHOOL OF SCIENCE & TECHNOLOGY

DEPARTAMENT OF PHYSICS

BEATRIZ AZEDO RATO ALVES CALADO

BSc in Biomedical Engineering

# 3D PRINTED HYDROGELS BASED ON POLYSACCHARIDES AND MAGNETIC NANOPARTICLES FOR BIOMEDICAL APPLICATIONS

MASTER IN Biomedical Engineering

NOVA University Lisbon

April, 2024

NOVA SCHOOL OF SCIENCE & TECHNOLOGY

DEPARTAMENT OF PHYSICS

# 3D PRINTED HYDROGELS BASED ON POLYSACCHARIDES AND MAGNETIC NANOPARTICLES FOR BIOMEDICAL APPLICATIONS

**BEATRIZ AZEDO RATO ALVES CALADO**

BSc in Biomedical Engineering

**Adviser:** Susete Maria Brazão Nogueira Fernandes
Assistant Professor, *NOVA University Lisbon*

**Co-advisers:** Paula Isabel Pereira Soares
Principal Researcher, NOVA University Lisbon

**Examination Committee:**

**Chair:** Célia Maria Reis Henriques,
Invited Assistant Professor, FCT-NOVA

**Rapporteurs:** Henrique Martiniano Vazão de Almeida,
Researcher, FCT-NOVA

**Adviser:** Susete Maria Brazão Nogueira Fernandes,
Assistant Professor, FCT-NOVA

MASTER IN BIOMEDICAL ENGINEERING

NOVA University Lisbon
April, 2024

**3D printed hydrogels based on polysaccharides and magnetic nanoparticles for Biomedical applications**

# ACKNOWLEDGMENTS

Queria começar por agradecer às minhas orientadoras, Professora Dr.ª Susete Fernandes e Professora Dr.ª Paula Soares, por me darem a oportunidade de trabalhar convosco. A exigência, determinação e curiosidade que me incutiram é inegável. Obrigada pela ajuda que me deram, dentro e fora do laboratório.

À muy nobre FCT, agradeço todas as experiências que me foram proporcionadas e o facto de nesta casa eu ter aprendido muito sobre tudo e mais alguma coisa, especialmente sobre mim própria. Nunca esquecerei este sítio onde fui me senti recebida de braços abertos desde o primeiro dia.

Após este tempo no 107, é seguro dizer que houve várias pessoas que marcaram o meu percurso e a quem devo um grande, grande obrigado. À Adriana, pelas aprovações casuais, conselhos académicos e fofoca ocasional; ao Cezar, pelas teorias discutidas às 7 da noite e piadas sobre a margem sul; à Bea Silva, por ser a minha mana do laboratório, sempre a rir da vida no geral e a atender telefonemas da secretaria super engraçados; à Dona Augusta, pelos desabafos ocasionais e ajudas sentidas; à Inês Santos, pelos cafezinhos e companhia. À Rafaela por ser um anjinho que me ajudou sempre de boa vontade. À Mariana, pelas boas receções ao laboratório 211 e à Inês por me ter feito companhia na impressora quando ainda precisava. E claro, não podia de mencionar a Teresa, que recebeu as minhas mil mensagens de marcação da impressora.

Um obrigado não chega para a minha família e amigos, que foram o melhor suporte que eu poderia alguma vez ter pedido neste percurso. Quero começar por agradecer à minha mãe, cujo suporte, força e abraço serão sempre o meu maior refúgio. Ao meu pai, pelas palavras de incentivo sempre presentes. Ao meu irmão Henrique, por ser um apoio com o melhor sentido de humor que eu conheço, sempre a alegrar-me o dia. Ao meu padrasto, pelas conversas motivacionais que vão sempre ajudar muito. Aos meus avós, Maria, Lizete e Francisco, aos meus tios, Nuno e Sandra, e claro, às minhas primas, Bruna e Inês, por sempre se preocuparem e ajudarem no que podem. Ao meu irmão Francisco, por uma relação com tanto carinho que significa muito para mim.

À Cristiana, a minha companheira de viagem Biomédica, um obrigado gigantesco pelos conselhos, conversas motivacionais, abraços (desde o dia um, naquele corredor antes da primeira aula de Biologia Molecular) e aventuras no geral. Sem ti, seguramente não teria sido a mesma coisa (muito menos piada teria tido, pelo menos). Um obrigado também à Catarina, Matilde e Bea, que me ajudaram a sentir em casa, a orientar-me e a sentir-me menos sozinha.

Ao Miguel, obrigada pelos cafezinhos, almocinhos e conversas motivacionais tão frequentes. És o meu melhor amigo e uma das pessoas que tenho há mais tempo comigo, o que me dá o maior dos orgulhos. Aos amigos da terra, Joana, Ana, Bia Lopes, Bia Raichande, Cat, David, Inês, Rúben, um obrigado pela vossa amizade, que significa mesmo muito para mim.
E claro, um grande grande grande agradecimento para (parafraseando uma lenda) aqueles que se vestem de preto comigo. O crescimento, autoestima e pujança que tenho hoje em dia existe, em grande parte, por vossa causa. Ajudaram-me a descobrir-me, a sair do mais fundo dos poços e a viver os melhores momentos que alguma vez vivi na faculdade e na vida. À Laires, amiga gráfica, cujo companheirismo, amizade e dedicação me enche de orgulho por ter alguém assim ao meu lado. Ao Tomás, a pessoa mais caótica, mais igual a mim e que mais me surpreendeu, o teu apoio tem sido tudo. Ao Noites, todo durão mas sempre com uma palavra amiga (ou não, o sentido de humor é importante). Ao Cristo, o meu companheiro velhote sempre disponível para dois dedos de conversa e piadas da bicha do demónio. À Peixoto, a voz da ponderação e da razão que eu sempre gostei tanto. À Bolinhas, a minha madrinha, a melhor que podia ter pedido, rainha do tough love e a melhor conselheira de todas. Sem vocês, não teria de todo sido o mesmo e agradeço todos os dias ter-vos na minha vida.
Por último, um gigantesco obrigado ao Diogo, o meu namorado. Não sei o que seria de mim sem o teu apoio, conforto e companhia. És a minha pessoa e eu tenho o maior dos orgulhos em ti e em nós. Amo-te muito.

Este trabalho foi financiado por fundos nacionais pela FCT - Fundação para a Ciência e Tecnologia, I.P., no âmbito dos projectos LA/P/0037/2020, UIDP/50025/2020 and UIDB/50025/2020 do Laboratório Associado i3N – Instituto de Nanoestruturas, Nanomodelação e Nanofabricação.

"Life need not to be easy, provided only that it is not empty" (Lise Meitner).

# ABSTRACT

Cancer is one of the most significant challenges humanity faces nowadays. The most commonly applied therapies, like chemotherapy, are not specific for tumour cells, causing systemic toxicity. Drug delivery systems are an approach to avoid these effects. Hydrogels, polymeric crosslinked matrices, are widely studied for this application due to their advantageous characteristics, like matrices porosity and swelling capacity. Hydrogels can be processed by 3D bioprinting, a technique to develop layer-by-layer structures through software-controlled bioink deposition, enabling customized systems for drug delivery applications. Hydrogels may also be coupled with Superparamagnetic Iron Oxide Nanoparticles (SPIONs). In a therapeutic approach named magnetic hyperthermia, these NPs cause the tumour temperature to rise when subjected to an Alternating Magnetic Field (AMF). This master thesis developed 3D bioprinted methacrylate chitosan (ChMA) hydrogels reinforced with Cellulose Nanocrystals (CNC) with SPIONs incorporated.

The successful methacrylation process of ChMA was confirmed through chemical characterisation, while thermal analysis indicated a lower decomposition temperature compared to chitosan. Subsequently, bioink formulations incorporating ChMA, CNC, and Irgacure 2959 as the photoinitiator were developed and assessed rheologically, demonstrating shear-thinning behaviour and increased viscosity with higher ChMA and CNC concentrations. Based on these findings, two formulations were selected for 3D bioprinting, with one yielding successful outcomes after optimization of printing parameters, UV light exposure, and photopolymerization mechanisms. This formulation was used to produce hydrogels using moulds for characterisation purposes. Mechanical tests on the obtained structures provided insights into their compression behaviour, while morphological analysis via Scanning Electron Microscopy (SEM) revealed a porous matrix with homogeneous CNC distribution. PBS absorption tests indicated rapid phosphate buffered saline uptake followed by stabilization. Despite initial attempts, the addition of SPIONs to the hydrogels was unsuccessful in achieving photocrosslinked structures. This work represents an early stage in the development of a novel 3D bioprinted system, encompassing material synthesis, bioink formulation, bioprinting processes and bioink and structure characterisation.

**Keywords**: 3D bioprinting, chitosan, nanocellulose, photocrosslinking, SPIONs

# RESUMO

O cancro é um dos maiores desafios da atualidade. As terapias mais frequentemente aplicadas, como a quimioterapia, causam muitas vezes toxicidade sistémica, pela falta de especificidade para as células tumorais. Os sistemas de administração de fármacos podem colmatar estes efeitos. Os hidrogéis, matrizes poliméricas reticuladas, são estudados para esta aplicação devido à sua porosidade e capacidade de inchamento. A impressão 3D, técnica que permite desenvolver estruturas através da deposição de tinta controlada por software, permite criar hidrogeis personalizados para administração de fármacos, com possibilidade de incorporação de nanopartículas de óxido de ferro superparamagnéticas (SPIONs). Estas podem ser utilizadas para hipertermia magnética, aumentando a temperatura no local do tumor. Esta dissertação focou-se em desenvolver hidrogéis de quitosano metacrilato (ChMA) impressos em 3D, reforçados com nanocristais de celulose (CNC) e com SPIONs incorporados.

O processo de metacrilação do ChMA foi confirmado através da caraterização química e a análise térmica mostrou uma temperatura de decomposição deste polímero mais baixa que a do quitosano. A avaliação reológica das formulações desenvolvidas de tinta de ChMA, CNC e Irgacure 2959 demonstrou um comportamento aparente de pseudoplástico e um aumento da viscosidade com o aumento das concentrações de ChMA e CNC. Com base nestas conclusões, foram selecionadas duas formulações para impressão 3D, com resultados favoráveis numa delas após otimização dos parâmetros de impressão, exposição à luz UV e mecanismos de fotopolimerização. Esta formulação foi utilizada para produzir hidrogéis com recurso a moldes, que foram submetidos a testes mecânicos, aferindo sobre o seu comportamento sob forças de compressão. A análise morfológica por microscopia eletrónica de varrimento (SEM) revelou uma matriz porosa com uma distribuição homogénea de CNC. Os testes de inchamento indicaram uma rápida absorção de PBS seguida de estabilização. A adição de SPIONs aos hidrogéis levou à não fotopolimerização, quer em impressão 3D ou hidrogéis em molde. Este trabalho mostra uma fase inicial no desenvolvimento de um novo sistema impresso em 3D, abrangendo a síntese de materiais, a formulação da tinta, os processos de impressão e a caraterização da tinta e da estrutura.

**Palavras chave:** Impressão 3D, quitosano, nanocelulose, fotopolimerização, SPIONs

# CONTENTS

# LIST OF FIGURES

# LIST OF TABLES

# ACRONYMS

| | |
|---|---|
| **3D** | Three dimensional. |
| **AMF** | Alternating magnetic field. |
| **ChMA** | Methacrylate chitosan |
| **CNC** | Cellulose nanocrystal |
| **CNF** | Cellulose nanofiber |
| **DSC-TG** | Scanning calorimetry with thermogravimetric analysis |
| **DTT** | Dithiothreitol |
| **FTIR-ATR** | Fourier-transformed infrared with attenuated total reflectance |
| **LAP** | Lithium phenyl-2,4,6-trimethylbenzoylphosphinate |
| **MA** | Methacrylic anhydride |
| **NP** | Nanoparticle |
| **PBS** | Phosphate buffered saline |
| **PEG** | Polyethylene glycol |
| **SEM** | Scanning electron microscopy |
| **SPION** | Superparamagnetic iron nanoparticle |
| **UV** | Ultraviolet region of the electromagnetic spectrum |

# SYMBOLS

| | |
|---|---|
| **Abs** | Average of absorbances. |
| **Fe** | Iron. |
| **HCl** | Hydrochloric Acid. |
| $\mathbf{m_{3D\ model}}$ | Measures performed in the 3D model. |
| $\mathbf{m_{3D\ bioprinted\ structure}}$ | Measures performed in the 3D bioprinted structure. |
| $\mathbf{N_2}$ | Nitrogen. |
| $\mathbf{S_w}$ | Swelling ratio. |
| $\mathbf{W_0}$ | Weight of the dried hydrogels. |
| $\mathbf{W_t}$ | Weight of the hydrogels in each time interval. |

# 1

# INTRODUCTION

This chapter provides a framework for the work carried out in this master's thesis, as well as a description of the system developed and its possible applications. Relevant information on the materials and techniques used is presented, as well as previous work in which they have been employed.

## 1.1 Context and Motivation

The World Health Organization defines cancer as a group of diseases in which abnormal cells grow out of control, passing their normal limits. This process can start in almost any organ and spread to adjacent organs or tissues in a process called metastasis, which is the main cause of death by cancer [1]. This condition is a rising global burden, with 19.98 million new cancer cases detected in 2022 and about 9.74 million fatalities reported in the same year [2]. By 2045, it is expected that the number of new cancer cases will reach 32.64 million, an increase of 63% since 2022, according to GLOBOCAN estimates [3]. In 2019, this condition was the primary or secondary cause of death in 112 out of 183 countries, with a population under 70 years [4], constituting a significant challenge to worldwide public health [5]. Chemotherapy is one of the most chosen therapeutic approaches for cancer treatment and recurrence prevention [6][4]. Chemotherapy agents are administrated in the bloodstream [7] and affect DNA replication and cell mitosis, which eliminates fast-growing and dividing cells. However, the drug is not applied exclusively to the tumour cells, leading to systemic toxicity, which results in adverse effects on healthy tissue. Additionally, since the drug is not focused on the tumour site, a higher dose is required, which is more harmful to healthy cells and leads to an increase in multiple drug resistance. Therefore, to overcome these issues, it is necessary to develop systems that deliver the therapeutic agents directly to the tumour region [6], improving its therapeutic efficacy [8].

One possible solution is drug delivery systems using hydrogels. These structures present a promising solution to the current drawbacks of drug delivery therapies, mitigating these challenges and augmenting the therapeutic effects of drugs at targeted sites. Their advantageous and adjustable characteristics for drug delivery include compatibility with aqueous

conditions, crucial for physiological environments, and a highly porous matrix that can transport and shield drugs from degradation. Moreover, their ability to swell and shrink enables control over drug release, maintaining high concentrations at targeted sites since the drug is loaded in the matrix, being released through diffusion when the aqueous environments contact with the hydrogel mesh. Taking this mechanism into consideration, the tunability of properties like the hydrogel porosity and swelling degree aids the adaptability of the system in terms of drug releasing and targeting to the required site [9]. Other useful qualities of hydrogels for biomedical applications include their improved biocompatibility due to their soft texture that resembles many soft biological tissues, which reduces the inflammatory response [10][11]. Combining hydrogels with 3D bioprinting is promising in drug delivery since it allows the design of systems in terms of shape and dosage, adapting them to the requirements of the targeted site [9]. The design and development of these customized systems is fast and avoids the population-centric approach, adapting the system features to each patient's specific needs. Besides that, additive manufacturing is more cost-effective since it is cheaper and requires less resources and effort [12].

Hyperthermia is another therapeutic approach for cancer treatment that takes advantage of the sensitivity of tumour cells to higher temperatures, which either sensitize them to other therapeutic approaches or kill them. However, it is challenging to efficiently target the temperature increase without damaging surrounding tissues [13]. Superparamagnetic nanoparticles (SPIONs) can generate heat when exposed to an alternating magnetic field (AMF) [14], having the potential to be used for hyperthermia. By incorporating SPIONs in a hydrogel matrix, it is possible to address the challenge of targeted heat application [13].

This master thesis aims to develop a 3D bioprinted multifunctional hydrogel system that combines the benefits of hydrogels and magnetic hyperthermia. To achieve this goal, a photocrosslinkable methacrylate chitosan (ChMA) hydrogel reinforced with cellulose nanocrystals (CNCs) and incorporating SPIONs was developed, a combination of materials not yet documented, to the best of our knowledge. Since the main goal was to be able to 3D bioprint the developed system, the formulation was optimized by varying the amount of polymer and reinforcement nanoparticles, as well as the printing parameters, conditions, and reaction mechanisms. This work is organized into four chapters: the first of which explains the theoretical concepts required to understand this work and provides a bibliographic review of the already existing work in this field. Next, in the second chapter, the materials used and methods performed in the laboratory are described, including the synthesis of the polymer, the formulation of the bioinks, the production of hydrogels, and the 3D bioprinting protocol. This is followed by the assessment of the results obtained from the chemical and thermal analysis of methacrylate chitosan, as well as the bioink's rheological behaviour, 3D bioprinting process, morphologic characterisation and mechanical and PBS absorption properties of the hydrogels. Finally, the conclusions and future perspectives of this work are presented in the last chapter.

The research work described in this dissertation was carried out in accordance with the norms established in the ethics code of Universidade Nova de Lisboa. The work described and the

material presented in this dissertation, with the exceptions clearly indicated, constitute original work carried out by the author.

## 1.2 Theoretical concepts

### 1.2.1 Hydrogels

Hydrogels are three-dimensional structures composed of hydrophilic polymeric chains that have been crosslinked, resulting in stable polymeric networks [11] capable of absorbing large amounts of water without dissolving [15].

The mechanical and biochemical properties of hydrogels are closely tied to their crosslinking method. Crosslinking methods are divided into physical crosslinking, in which reversible bonds are formed between chains, and chemical crosslinking, which forms stronger, permanent covalent bonds, resulting in hydrogels with enhanced stability, mechanical properties, and adjustable degradation. Photocrosslinking is a chemical crosslinking method that can be triggered by light exposure and requires the presence of acrylate or methacrylate groups and a photoinitiator. It offers several advantages, including the fact that it is a quick process that occurs at room temperature in mild conditions [15], precise control over hydrogel properties through reaction management (e.g., controlling the exposure time or distance to the light) [16], and targeted reaction areas via selective light exposure [15]. However, drawbacks of this method include the cytotoxicity of certain photoinitiators and the potential for unwanted reactions involving free radicals formed during the process [16].

### 1.2.2 Chitosan

Chitosan is obtained through partial deacetylation of chitin (degree of deacetylation of 50% or higher [17]), a natural polysaccharide extracted from crustacean shells [11][18]. Chitosan chains are formed by *N*-acetyl-glucosamine and deacetylated D-glucosamine, randomly distributed and bonded by β-(1–4)-glycosidic bonds. This distribution produces a structure containing amino groups, positively charged, as well as primary and secondary hydroxyl groups, also positively charged, making it a cationic polysaccharide capable of interacting with negatively charged biomolecules in the body. This contributes to the many advantageous properties of this polymer in the biomedical field, such as biocompatibility, biodegradability, anti-inflammatory properties, and antioxidant effects [19]. Besides that, it is an easy-to-modify polymer since it has plenty of free amino groups [20]. A disadvantage of this polymer is the tendency of the amino groups to protonate at neutral pH, allowing interaction between them and the polar part of the molecule, which limits its solubility in water. Biocompatible, flexible, and hydrophilic hydrogels are obtained from chitosan. They are vastly used in the biomedical field as drug delivery systems, injectables, 3D bioprinted biomaterials, absorbable sutures, among others [18].

### 1.2.3 Methacrylate chitosan

To produce photocrosslinkable hydrogels from chitosan, methacrylation of the polymer was required, achievable through reaction with methacrylic anhydride (MA), for example, which is an advantageous option in the biomedical field because of its mild solubility in water. However, it must be employed in small amounts due to its toxicity [18]. Upon reaction with MA's methacryloyl groups, chitosan's amino groups [19] transform into methacrylamide groups, allowing photocrosslinking in the presence of a photoinitiator [21] such as 2-Hydroxy-4'-(2-hydroxyethoxy)-2-methylpropiophenome (Irgacure 2959), which is well tolerated by various cell types [15]. This modification also improves chitosan's solubility in water [22].
Photopolymerization with Irgacure 2959 is triggered by UV light of 365 nm and can proceed via two mechanisms: chain growth and step growth reactions, both displayed in Figure 1-1. In chain growth (left panel Figure 1-1), Irgacure 2959 generates free radicals under UV exposure, initiating the chain reaction by reacting with ChMA's alkene groups, forming a carbon-centred radical that reacts with other alkene groups, forming growing chains. However, the presence of oxygen inhibits this mechanism (3rd schematic reaction). Alternatively, step growth reaction (right panel Figure 1-1) requires the presence of thiol groups, where the photoinitiator, upon UV light exposure, forms a radical that reacts with a thiol group, abstracting a proton and forming a thiyl radical. This agent combines with the alkene group of a ChMA, resulting in a carbon-centred radical that reacts with another thiol group, abstracting a proton and forming a new thiyl group as well as a monomer. This monomer will bond with other monomers to build a crosslinked network. Chain and step growth mechanisms may occur simultaneously [23].

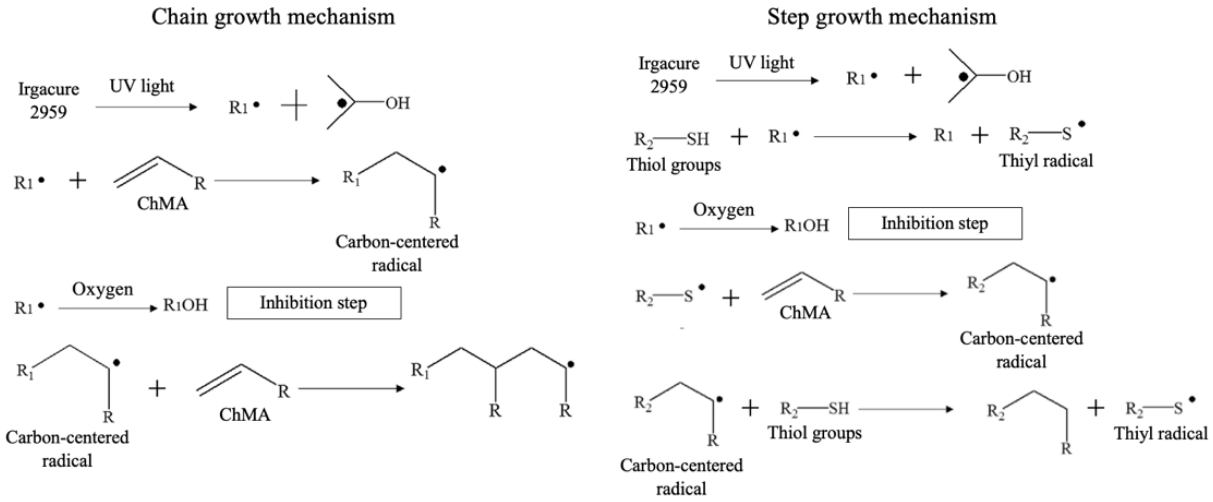


Figure 1-1 - Schematic representation of photopolymerization mechanisms of ChMA with the photoinitiator Irgacure 2959. Adapted from [23].

### 1.2.4 Cellulose Nanocrystals (CNC)

Methacrylate chitosan hydrogels suffer from a major drawback, this is insufficient mechanical strength. Incorporating nanofillers or other polymeric materials into their matrix effectively

addresses this issue [24]. Cellulose nanocrystals (CNCs) are a popular reinforcing agent due to their excellent features, including enhanced mechanical strength, biocompatibility, large surface area, low toxicity and density, high aspect ratio, and biodegradability [25].
Cellulose is a widely abundant natural polymer consisting of linear chains of cellobiose units linked by b-1,4-linkages. Individual chains are organized into fibres due to hydrogen bonds between intermolecular hydroxyl groups and hydrophobic interactions. This results in an organized, tight-packed polymer, leading to its semicrystalline nature. Because of these aspects, cellulose has enhanced strength and flexibility. The fibres have crystalline and amorphous regions [26]. Mechanical shear or controlled acid hydrolysis of cellulose leads to the split of fibres at amorphous points, forming nanocellulose comprising rod-shaped, elongated fibrillar particles. Depending on the fibre's deconstruction technique and source, different types of nanocellulose with variable chemical and physical characteristics are obtained. CNC are obtained through acid hydrolysis of cellulose, which destroys more amorphous regions of the fibres, resulting in a very crystalline structure with improved rigidity compared with other types of nanocellulose [27] [26].
A nanocomposite can be achieved by blending chitosan, a cation, and nanocellulose, an anion, creating a polyelectrolyte complex due to their opposing charges, in aqueous environments. The primary interaction between these polymers is strong electrostatic interactions, but hydrogen bonding, hydrophobic interactions, dipole interactions, and van der Waals forces also occur [28].

### 1.2.5 Superparamagnetic Iron Oxide Nanoparticles (SPIONs)

The behaviour of magnetic materials is categorized through their magnetic susceptibility, which is the correlation between the applied magnetic field and the induced magnetization in the material. Graphically, a hysteresis loop results from this ratio, featuring two main parameters: remanence, which is the magnetization that lasts after the exposure to a magnetic field and its removal; coercivity, which is the magnitude of the magnetic field necessary to reverse the magnetization saturation of a material to zero [29].
Iron oxide nanoparticles are the most used magnetic nanoparticles in the biomedical field since they are biocompatible and stable [29]. Magnetite ($Fe_3O_4$) is an iron oxide constituted by $O^{2-}$ anions and iron cations in two different valence states, $Fe^{2+}$ and $Fe^{3+}$. When the size of the magnetite particles is reduced to nanoscale, the most energetically favourable magnetic organization is the formation of a single domain, uniform in terms of magnetization. When exposed to a magnetic field, all the magnetic moments of the nanoparticles align with it. When it ceases, the magnetic properties of the material cease as well, presenting no remanence, hysteresis and a coercivity of zero. These are typical features of superparamagnetic behaviour [14][29].
When subjected to an alternating magnetic field (AMF), SPIONs are able to generate heat, a feature applied in cancer treatment through magnetic hyperthermia. This therapy elevates the tumour temperature to 39°C - 45°C, potentially destroying or sensitizing tumour cells to other treatments due to their vulnerability to heat. Tumour cell damage caused by this approach

includes DNA repair interference, cell membrane fluidization, programmed cell death induction, protein denaturation, and alteration of the tumour microenvironment. A significant advantage lies in its precise targeting, affecting only the area containing SPIONs exposed to an AMF, forcing the need for nanoparticles contained delivery systems [14]. One solution involves incorporating nanoparticles into a hydrogel matrix, achieved through permanent chemical interactions or physical interactions between the hydrogel and the SPIONs, the approach aimed in this study [30]. The remaining challenges include optimizing structures with SPIONs in terms of behaviour under AMF, material selection, size, shape, concentration, biocompatibility when not under AMF, achieving tumour site specificity and determining ideal AMF parameters for effective application [14].

### 1.2.6 3D bioprinting

3D bioprinting enables the precise fabrication of complex structures layer-by-layer using software-controlled bioink deposition [31][32]. Extrusion-based bioprinting involves continuous filament extrusion from a syringe nozzle under constant extrusion force onto a substrate to form desired shapes. This technique is widely used because of its cost-effectiveness and versatility, being able to 3D bioprint bioinks featuring a wide range of viscosities as well as bioinks containing cells in various concentrations. The path followed by the nozzle is controlled by the printing software, which creates the digital model with the selected configurations. Printing parameters such as nozzle diameter, pressure and speed significantly influence the process. A piston-driven system, applied in this study, employs the rotational movement of a motor-connected guided screw to linearly push the piston for bioink dispensing [33].
An appropriate bioink is crucial for 3D bioprinting, with suitable biocompatibility, mechanical properties, printability [33] and rheological behaviour [34]. Hydrogel precursor solutions are among the materials typically used as bioinks [33]. Fast stabilization and crosslinking of the layers are desired, preventing bioink flow before crosslinking, gravity, and surface tension-caused deformation of the bioprinted filaments, leading to differences from the desired design. This can be achieved using hydrogels with fast crosslinking ability and improved rheological behaviour, for instance, bioinks with higher viscosities [34], obtaining more structural support. Additionally, shear-thinning behaviour, where the viscosity decreases with increasing shear stress in non-Newtonian fluids, aids in smoother bioink extrusion [33]. Photocrosslinking is popularly used for stabilizing the filaments during or after the bioprinting process, the second one requiring bioinks with higher shape retention [34].
This crosslinking technique offers several advantages in this process, including the previously mentioned promptness, mild operating conditions, spatiotemporal and intensity control, and the ability to manipulate hydrogel properties through reaction management. Besides that, light can be easy to apply in the bioprinting process. In contrast, methods involving crosslinking via pH or temperature may be reversible under different pH or temperature conditions, which is typically not the case with light-induced crosslinking [35].

## 1.3 State of the art

In the last years, several systems featuring the above-mentioned materials have been developed in the biomedical field, for different applications. Starting with systems for drug delivery, Bozuyuk *et al*., describe the development of methacrylamide chitosan microswimmers incorporating SPIONs and the phenyl-2,4,6-trimethylbenzoyl-phosphinate (LAP) photoinitiator. Their double-helicoidal shape was 3D bioprinted through two-photon direct laser writing and photopolymerized. When exposed to a rotational magnetic field, these structures exhibited controllable movement, which is advantageous in delivering the drug to the pretended local. The drug-carrying and releasing were performed through the functionalization of the structures with a photocleavable group with a model drug attached. When subjected to UV light of a specific wavelength, these groups undergo cleavage, releasing the drug-functionalized segment from the backbone structure. This process is controllable by adjusting parameters such as light intensity, exposure duration, and the targeted area. Limitations of this system included partial penetration of UV light in skin and water-based systems [21].

The materials employed in the system developed in this work can be applied for drug delivery applications in other forms besides hydrogels. For instance, Sumitha *et al.* reported a pH-dependent drug release system by conjugating SPIONs and the model drug Doxorubicin with another type of nanocellulose, nanofibrilated cellulose (CNFs). This system exhibited the ability to undergo magnetic hyperthermia when subjected to an Alternating Magnetic Field (AMF). Notably, it could penetrate cells and release the drug with a higher release rate in acidic environments. The samples showed high magnetization values, which allows targeted delivery of the drug when exposed to an external magnetic field, minimizing its dispersion while ensuring precise dosage application. This was supported by the tendency of the system to accumulate in and around the cellular membrane, which also facilitated the targeted hyperthermia process [36].

In the field of tissue engineering applications, polymeric 3D bioprinted structures allow the printing of scaffolds for cell adhesion and development of structures with embedded cells. Taking a look at some examples, in the work of Maturavongsadit *et al*. a thermocrosslinkable cell-encapsulated bioink for 3D bioprinting of scaffolds for bone tissue engineering and regeneration was developed. The bioink was constituted of chitosan with incorporated CNC with β-glycerol phosphate and hydroxyethyl cellulose as the crosslinking agents. β-glycerol phosphate promoted post-bioprinting thermocrosslinking at 37 ºC while hydroxyethyl cellulose enabled pre-bioprinting chemical crosslinking, enhancing shape retention of the bioprinted structures, as illustrated in Figure 1-2. CNC improved the mechanical properties of the bioink and its viscosity, which was also enhanced by cell presence. The bioprinting process did not affect cell viability, creating scaffolds that promoted osteogenic differentiation, improved by CNC presence [37].

Another system destined for tissue engineering was presented in the research conducted by Shen *et al*., a ChMA bioink was formulated for 3D bioprinting using a different bioprinting technique, Digital Light Processing. The photoinitiator LAP was selected taking into

consideration its lower cytotoxicity upon light exposure and faster crosslinking time, which decreased cytotoxicity as well. ChMA with a higher degree of substitution was used because it reduced crosslinking time and a lower ChMA concentration to achieve the required lower viscosity for this bioprinting technique. Well-defined and precisely patterned hydrogels were developed, with cell viability not affected by the bioprinting and photocrosslinking processes [38]. Osi *et al*. developed 3D bioprintable ChMA and methacrylate gelatin hydrogels incorporating nanohydroxyapatite and the photoinitiator Irgacure 1173, displayed in Figure 1-3A. Methacrylate gelatin becomes more viscous as temperature increases, so a heated printing head was utilized to aid extrusion. In the cooler printing bed, each layer thermocrosslinked, enhancing shape fidelity and structural stabilization. Subsequently, the bioprinted structures, with photocrosslinking abilities due to the presence of the methacrylate polymers, were exposed to UV light, resulting in improved hydrogel's mechanical properties. The shape fidelity of the hydrogels increased with methacrylate gelatin's concentration, polymer that also influenced the structural stability of the structure, decreased structure degradation in the physiological environment, improved its mechanical properties and contributed to the favourable environment to cells provided by the scaffolds. Nanohydroxyapatite only had minor contributions to the hydrogels [39]. Lastly, in the work of Tonda-Turo *et al*., cell-encapsulated ChMA and β-glycerol phosphate hydrogels featuring LAP as the photoinitiator were 3D bioprinted. The results can be observed in Figure 1-3B, C. Taking advantage of the thermocrosslinking ability of the hydrogels due to β-glycerol phosphate presence, in opposition to the previous work, the printing head had a lower temperature while the printing bed was warmer, facilitating a fluid extrusion and thermocrosslinking of each layer directly on the printing bed, increasing the retention of the structure shape. The structure was exposed to UV radiation between layers to allow photocrosslink, enhancing its stability. The bioprinted hydrogels promoted cellular growth and organization and exhibited high resolution [40].

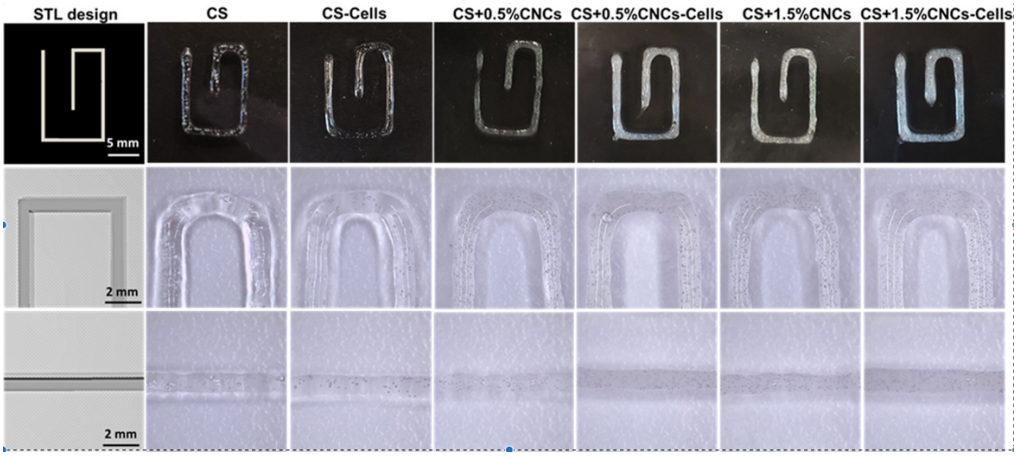


Figure 1-2 - The various designs of 3D bioprinted hydrogels in [37], with different formulations, and their respective CAD file (in the left side of the panel), for comparison.

A system with potential for both drug delivery and tissue engineering fields was developed by Ko *et al*. based on glycol chitosan and oxidized hyaluronate to develop a 3D bioprinted hydrogel incorporating SPIONs. The crosslinking of this system occurred due to the mix of

glycol chitosan and oxidized hyaluronate, and its self-healing properties allowed a subsequent bioprinting process without requiring post-crosslinking, as the hydrogel properties recovered after extrusion. The SPIONs concentration was chosen carefully since the results showed that higher concentrations could interfere with the crosslinking process. It was possible to modify the obtained structure when exposed to a magnetic field, with the hydrogel returning to its original shape when the stimulus ceased, which showed the potential of acting as a magnetically controlled system [41].

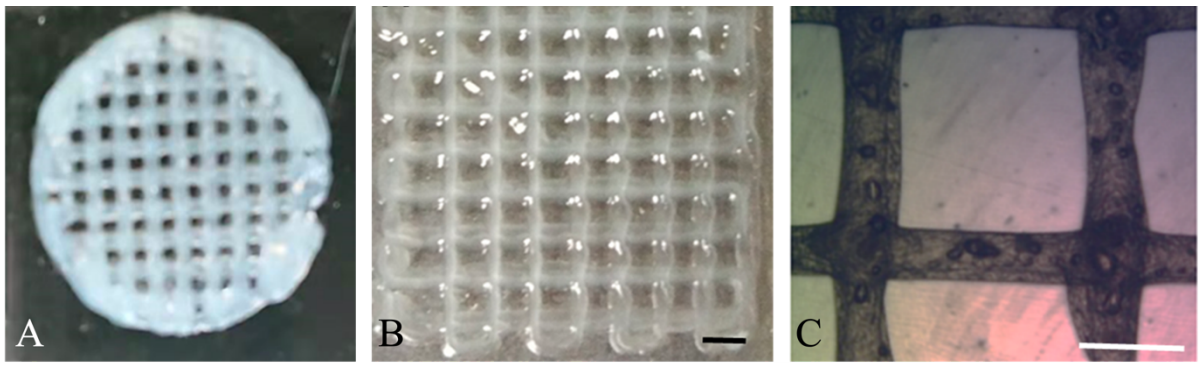


Figure 1-3 – A - hydrogel obtained in [39], after thermocrosslinking and photocrosslinking. B, C - 3D bioprinted structures obtained in [40] after bioprinting, in which thermocrosslinking occurred in the printing bed. In C, a zoomed-in view of the structure pores is presented. Scale bars: 1 mm.

Exploring alternative applications of similar hydrogel systems, in the work of Patel *et al*., 3D bioprinted, photocrosslinked ChMA hydrogels incorporating spherical nanocellulose, β-glucan and LAP as photoinitiator were developed for hydrogel sensor applications. The transparent nature of the resulting hydrogel facilitated precise sensor placement and enhanced device aesthetics. It featured adhesive properties, which prevent the need for extra materials to secure the device. Shape memory, shape recovery and self-healing properties that safeguard against damage and prolong equipment lifespan were validated. The hydrogel exhibited antimicrobial properties, enabling the use of this system in wearable electronic sensors without the need for antibiotics. The composite hydrogels also demonstrated enhanced conductivity, attributed to the formation of an efficient pathway for ion conduction within the hydrogel upon the application of voltage, which corresponds to an electrical current. This current was verified to successfully restore in healed zones (after damage) of the hydrogel. In terms of applications of this system, it was verified that increasing strain on the hydrogel led to increasing resistance and consequently decreased current on the hydrogel. This resulted in fluctuations of the measured current when attached to parts of the body that bent and stretched, showing the possibility of application in a real-time motion sensor. Successful incorporation into a writing detection system demonstrated its ability to detect intricate movements. It was also able to detect temperature. Due to the high hydroxyl group content and porous matrix, the hydrogel was also able to generate current in moist conditions, increasing with prolonged soaking [24].
In the work of Zhu *et al*., the potential for wound dressing applications of these systems is explored, with the development of a pH-responsive ChMA hydrogel featuring Irgacure 2959 as the photoinitiator. The wound healing process has a dynamic pH, which combined with

chitosan's swelling at decreased pH led to a hydrogel capable of releasing anti-inflammatory and antibiotic substances in the initial acidic phase, without overgrowth in the following proliferation stage. In this study, the hydrogels were obtained through different photopolymerization reactions featuring ChMA and Irgacure 2959, chain growth, step growth and a mix of both. This led to different crosslinking densities, tunable mechanical properties and swelling ratios as well as different pH sensitivities, demonstrating its ability to respond to different phases of wound healing. Although hydrogels were biocompatible, cellular adhesion and proliferation were not verified [23].

Innovative methods for 3D printing of structures are still found, like the 3D printed chitosan and CNC structure method presented in the work of Lin *et al*. The study showed that by combining polyethylene glycol (PEG) and CNC dispersion with a dextran and chitosan solution, inherently immiscible, a chitosan-CNC complex forms at the interface between the two solutions. This process occurs rapidly, enabling the fabrication of robust and flexible tubular structures when printing the chitosan-dextran solution in the CNC-PEG dispersion. Furthermore, this membrane was verified to successfully remove heavy ions from solutions, adsorbing them and facilitating their removal [42].

After reviewing previously developed work in this field, it is evident that hydrogel systems are extensively explored across various branches of the biomedical sector, and the biomaterials utilized in this study are widely applied. This bibliographic research also indicates that, to the best of our knowledge, the system presented in this master thesis is a novel approach, featuring a combination of biomaterials and techniques that has not been explored until now. The following sections will provide a more in-depth examination of the work conducted to develop this innovative system.

# 2

# MATERIALS AND METHODS

In this chapter, an overview of the used materials is presented, as well as the employed techniques to synthesize the utilized polymer and SPIONs, formulation of the bioinks, 3D bioprinting, production of hydrogels using moulds and characterisation of the obtained polymer, bioinks and structures.

## 2.1 Materials

The synthesis of ChMA was performed using chitosan of low molecular and degree of deacetylation 75.5% supplied by Cognis, acetic acid glacial (≥ 99.8%) from Carlo Erba, methacrylic anhydride (MA) with 2000 ppm topanol A as inhibitor (≥94.0%), was supplied by Aldrich and polyethylene glycol (PEG) with molecular weight of 35 kDa was purchased from Sigma.
For the synthesis of SPIONs it was used iron (III) chloride hexahydrate ($Fe_3O_4 \bullet 6\ H_2O$), hydroxyalamine ($HONH_2 \bullet HCl$) and phenanthroline ($C_{12}H_8N_2$) all supplied by Sigma-Aldrich, iron (II) chloride tetrahydrate 98\% ($FeCl_2 \bullet 4\ H_2O$) produced by Thermoscientific, ammonium hydroxide solution ($NH_4OH$), purchased from Honeywell, hydrochloric acid (HCl) 37% produced by Honeywell Fluka and ammonium acetate ($C_2H_7NO_2$) produced by Scharlau.
For the bioinks formulation commercial colloidal suspension of CNC from CelluForce NCC NCV100-NAL90, lot# C1A21029, was used as received, Irgacure 2959 (2-Hydroxy-4′-(2-hydroxyethoxy)-2-methylpropiophenone) and DL-Dithiothreitol (DTT), ≥99.0% from Sigma-Aldrich were used as well.

## 2.2 Methods

### 2.2.1 ChMA synthesis

The following procedure was based on a protocol previously described by Sayyar *et al.* [43]. 400 mL of chitosan solution 1.3% (w/w) in a solution of acetic acid 4% (V/V) was left stirring overnight at room temperature. Then, 25 mL of methacrylic anhydride (MA) was added dropwise under mechanical stirring. The reaction was performed protected from light for 24 hours

at 60 ºC. Finally, the obtained solution was dialysed against type II ultrapure water using a 12-14 kDa dialysis membrane, supplied by Spectra/Por, for 15 days. The solution was freeze-dried afterward. This synthesis was done on a larger scale, doubling the used quantities.
Microscopic images of the polymer sample were captured using an Olympus BX51 Optical Microscope with polarized light and an attached Olympus DP73 camera. The equipment featured a Scott KL2500 light source, and image acquisition was facilitated by Olympus Stream Basic 1.9 software. Additionally, macroscopic images of the polymer were acquired using a Nikon 1 J5 camera.

## 2.2.2 SPIONs production

### 2.2.2.1 Synthesis of iron oxide nanoparticles

The following method was described by Soares *et al*. [29]. First, 1.3515 g of iron (III) chloride hexahydrate and 0.497 g of iron (II) chloride tetrahydrate 98% were weighted. These salts were mixed with 100 mL of type II ultrapure water in a round-bottom flask. The stirring was performed mechanically, adding gaseous nitrogen ($N_2$) through a hose in a closed system.
10 mL of ammonium hydroxide solution was added using a syringe. After 5 minutes, the reaction was stopped. The solution was transferred to a beaker, using water to remove the remaining solution from the walls of the flask.
A strong magnet was placed in the bottom of the beaker so the nanoparticles precipitated. With a syringe, the supernatant liquid was removed. Four washes were performed.

### 2.2.2.2 Measurement of iron concentration

The phenanthroline method, described by Soares *et al*. in [29] was used to determine the iron concentration in the solution. First, a dilution with a ratio of 1:500 was made with the previously obtained SPIONs suspension. Then, to 40 µL of the dilution were added 20 µL of HCl. Five samples were produced. It sat for 1 hour, at room temperature. Afterwards, 10 mL of hydroxylamine solution (100 mg $mL^{-1}$) was produced through the addition of 1 g of hydroxylamine to 10 mL of HCl; 20 mL of phenanthroline solution 3 mg $mL^{-1}$ was made through the adding of 0.6 g of phenanthroline to 20 mL of HCl and 50 mL of ammonium acetate solution 500 mM were made through the adding of 1.297 g of ammonium acetate to 50 mL of HCl. These solutions were added to each sample in the following quantities: 100 µL of hydroxylamine solution, 500 µL of phenanthroline solution and 1140 µL of ammonium acetate solution. The absorbance of the samples was measured in the spectrophotometer UV-VIS (T90+ UV/VIS Spectrometer PG Instruments Ltd), using the solvent of the solutions as a baseline.

## 2.2.3 Bioink preparation

General procedure: first, the calculated amounts of synthesised ChMA, acetic acid and type II ultrapure water were mixed and stirred overnight. This mixture was sonicated (Hielscher UP400St) until a homogeneous solution was obtained. The CNC suspension was sonicated as

well, providing 55 kJ/g of CNC to obtain a dispersed suspension. Then, the CNC suspension was added to the ChMA solution, under vigorous magnetic stirring. The mixture was left stirring until a homogeneous appearance was achieved. Next, the photoinitiator, Irgacure 2959, was added to the suspension in a proportion first described by Sayaar *et al*. [43], 12% (w/w) relative to the ChMA. It underwent magnetic stirring overnight, protected from the light, and afterwards, the mixture was put in the ultrasonic bath for 5 minutes. Formulations featuring two different ChMA concentrations, 2% (w/w) and 3% (w/w) were prepared with different CNC content. The amount of acetic acid, 3% (w/w), was constant. The formulations are presented in Table 1.

Table 1 - ChMA and CNC concentrations for the different bioink formulations.

| **ChMA concentration (w/w)** | **CNC concentration (w/w)** |
|---|---|
| 2.0% | 0.0% |
| | 1.5% |
| | 3.0% |
| | 5.0% |
| 3.0% | 0.0% |
| | 0.5% |
| | 1.0% |
| | 1.5% |
| | 2.0% |

The addition of DTT was made before each 3D bioprinting or hydrogel production with moulds session. The amount of DTT added corresponded to 6.7% (w/w) relative to Irgacure 2959. It was added in the dark, with vigorous stirring with a spatula for 20 minutes.
Formulations with SPIONS: the synthesised SPIONs suspension was added to the bioink in a proportion of 10% (w/w) relative to ChMA. The mixture was stirred with a spatula for 10 minutes.

### 2.2.4 3D bioprinting

The 3D bioprinting process was performed in a TissueLabs bioprinter, the TissueStart Model TSST-V1. The structure's design was made in Blender, a free open-source 3D modeling software, and the projects were extracted in the form of .STL files. A preview of the 3D models used is illustrated in Figure 4-2 of the Annex A.2. These files were read by the bioprinter software and sliced using Slic3r, an online software connected to the bioprinter software. Several printing parameters were explored, which are explained in the Results section.
The bioink was placed in a 5 mL syringe, isolated from light with black tape, and placed in the bioprinter holder in a dark environment. The holder was isolated with aluminium foil. A

Professional Nail Lamp produced by BLUEQUE, model BLUEQUE V7 with LED lamps of 365 and 405 nm, was held with claws and universal supports near the printing plate. The bioprinter was covered with a blackout cloth during the bioprinting process. The structures were bioprinted on a glass substrate with UV light irradiance. After bioprinting, the structures underwent UV light exposure. To evaluate if the photocrosslinking had occurred, a spatula was used to assess the rigidity of the structures. Then, the photograph documentation of the structures was made using a camera Nikon 1 J5. Afterwards, the structures were washed 5 times using type II ultrapure water and kept in water in polystyrene dishes at room temperature.

### 2.2.5 Production of hydrogels using moulds

The bioink placement in the syringe was performed similarly to the 3D bioprinting procedure. The bioink was placed in a transparent acrylic mould with cylindrical holes, previously glued to a plastic substrate and exposed to UV light. Aiming to assess the occurrence of photocrosslinking, the rigidity of the structures was evaluated using a spatula. The photocrosslinked hydrogels were removed from the mould and washed 5 times in type II ultrapure water. Then, they were placed in polystyrene dishes and kept at room temperature.

### 2.2.6 Characterisation

Several characterisation techniques were employed to characterise ChMA, the bioink formulations and the hydrogels produced with moulds. For the ChMA chemical and structural analysis, fourier-transformed infrared with attenuated total reflectance (FTIR-ATR) and scanning calorimetry with thermogravimetric analysis (DSC-TG) were performed. All bioink formulations were subjected to rheologic characterisation and the hydrogels produced with moulds underwent PBS absorption and mechanical tests. Scanning electron microscopy (SEM) analysis was conducted to assess the morphology of the hydrogels. Additional in-depth details regarding the techniques executed, experimental parameters, equipment employed, and sample preparations are available in Annex A.1.

# 3

# RESULTS

This section presents the obtained results and their subsequent discussion. Initially, the occurrence of the methacrylation process is confirmed through the chemical characterisation of the polymer, alongside an assessment of its thermal behaviour. Subsequently, observations made during the synthesis, bioink formulation, SPIONs production, and bioink formulation are analysed. This is followed by an evaluation of the flow behaviour of the bioinks via rheological assessment. The printing parameters and their influence on this study are then delineated, succeeded by the characterisation of hydrogels derived from the selected bioink formulation. This involves mechanical and PBS absorption tests, as well as morphological analysis using SEM, marking the preliminary steps in the characterisation of this innovative system.

## 3.1 ChMA synthesis

The presented ChMA had an optimization path during this work. A first version was implemented based on the procedure described by Maiz-Fernández *et al* [20]. The procedure was similar to the one explained in the section Materials and methods, however, the reaction proceed at a lower temperature, 40 ºC instead of 60 ºC; the dissolution of chitosan was made in an acetic acid solution of lower concentration, 0.5% (V/V) instead of 4% (V/V), and the amount of methacrylic anhydride (MA) added was much superior, a ratio of 1:20 (Ch:MA) instead of 1:5 (Ch:MA). The obtained result was a non-homogeneous solution, with a white aggregate floating, which could be attributed to incomplete methacrylation of the chitosan backbone, leading to aggregates of MA since it only presented a mild solubility in water. This solution was dialysed and freeze-dried. The obtained polymer did not have the expected cloudy appearance and exhibited a solid smell to MA. The further dissolution of this product was very difficult, even with the addition of acetic acid, which typically dissolves non-functionalized chitosan. This was not the expected outcome since the methacrylation process was supposed to increase chitosan's dissolution at neutral pH [44]. The obtained outcome is possibly due to an uneffective methacrylation process, leading to unreacted MA present in the obtained polymer. This would explain the strong MA smell and the difficulty in dissolving the polymer.

An alternative to freeze-drying was also tried due to the low availability of the equipment and the high concentration of MA in the first version of the synthesis, which could damage the equipment. This approach aimed to create a highly concentrated ChMA solution out of the product solution, after dialysis. To achieve this, the membrane containing the solution was immersed in a PEG aqueous solution (~20% w/w), which has higher water affinity and can remove water from solutions. However, if the membrane was left too long on PEG, some parts would concentrate more and form solid aggregates of ChMA sticking to the membrane being impossible to remove. Therefore, the desired high concentration could not be obtained with this procedure alone. To solve this problem, from PEG the solution was placed in a rotary evaporator. However, this approach also failed to produce a solution with a high concentration of ChMA, as well as having several problems such as being impractical, time-consuming and difficult to control. Thus, this approach was abandoned.

Some adjustments were made to obtain the final procedure based on Sayyar *et al.* [43]. The reaction temperature was increased to 60 ºC, chitosan was dissolved in a solution with a higher concentration of acetic acid, 4% (w/w), and the added MA was substantially reduced to a ratio of 1:5 (Ch:MA). The problems mentioned above were eliminated with these changes, resulting in a cloudy, shiny, odourless polymer after dialysis and freeze-drying. Its solubility in water was also increased. Figure 3-1A illustrates the result show a photograph of the solid ChMA. Microscopic images can also be seen in Figure 3-1B, showing the birefringence of the fibers, characterised by varying refractive indices along different light propagation directions. This property is a sign of organization of the polymeric chains [45], however, in previous works, it was observed that the crystallinity of chitosan is decreased in the methacrylation process [43][46]. Therefore, further evaluation of the obtained polymer crystallinity is required. Furthermore, this property may be worth exploring since it is common to one of the predominant constituents of biological tissues: collagen [46].

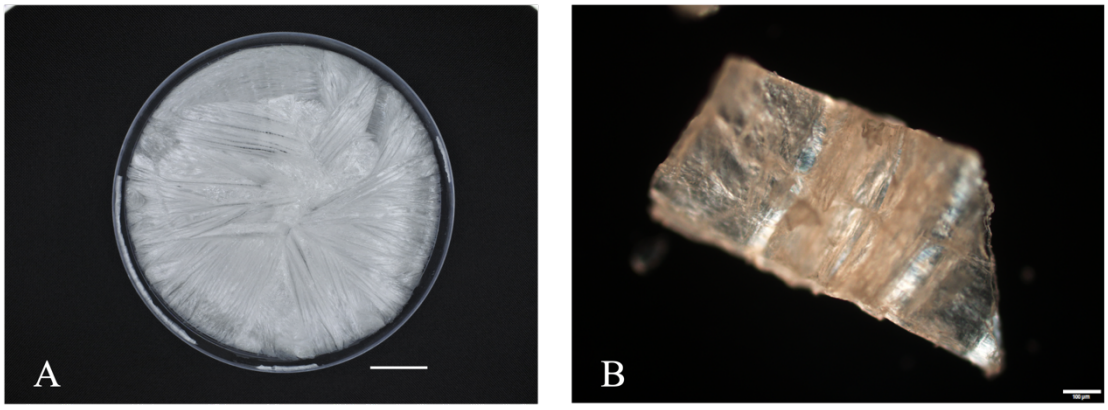


Figure 3-1 - A - Macroscopic view of synthesised ChMA Scale bar: 20 mm. B – Optical microscope image with crossed linear polarisers of synthesised ChMA. Scale bar: 100 μm.

## 3.2 Chemical and thermal characterisation of ChMA

### 3.2.1 Fourier-transformed infrared with attenuated total reflectance (FTIR-ATR)

The chemical analysis of chitosan and ChMA was conducted utilizing FTIR-ATR spectroscopy. The method identifies specific functional groups inside substances using their characteristic absorption bands. This is particularly significant in this context as it enables the confirmation of the occurrence of the methacrylation process. The spectra of both chitosan and methacrylate chitosan are presented in Figure 3-2, with the common bands between them highlighted. Figure 4-1, in Annex A.2, displays the FTIR-ATR spectra of chitosan, presented in two zoomed-in images, where chitosan's typical absorption bands can be observed. The band at 3357 $cm^{-1}$ corresponds to the overlapping of O-H and N-H stretching, followed by the band at 2875 $cm^{-1}$, originated from the C-H stretching. The absorbance bands at 1646 $cm^{-1}$ and 1587 $cm^{-1}$ are attributed to amide II, to acetyl group C-O stretching and N-H bending, respectively. Next, it is possible to observe the band associated with $-CH_2$ at 1416 $cm^{-1}$, asymmetrical C-H bending of the $CH_2$ group at 1374 $cm^{-1}$ and amide III at 1318 $cm^{-1}$. The bands associated with the C-O-C bridge, its asymmetrical stretch, the skeleton vibrations implying C-O-C stretching bands, and C-O-C stretching of the glycosidic bond, are respectively at 1149 $cm^{-1}$, 1026 $cm^{-1}$, and 892 $cm^{-1}$. The band at 1061 $cm^{-1}$ is due to the C-N stretching vibration mode [29].

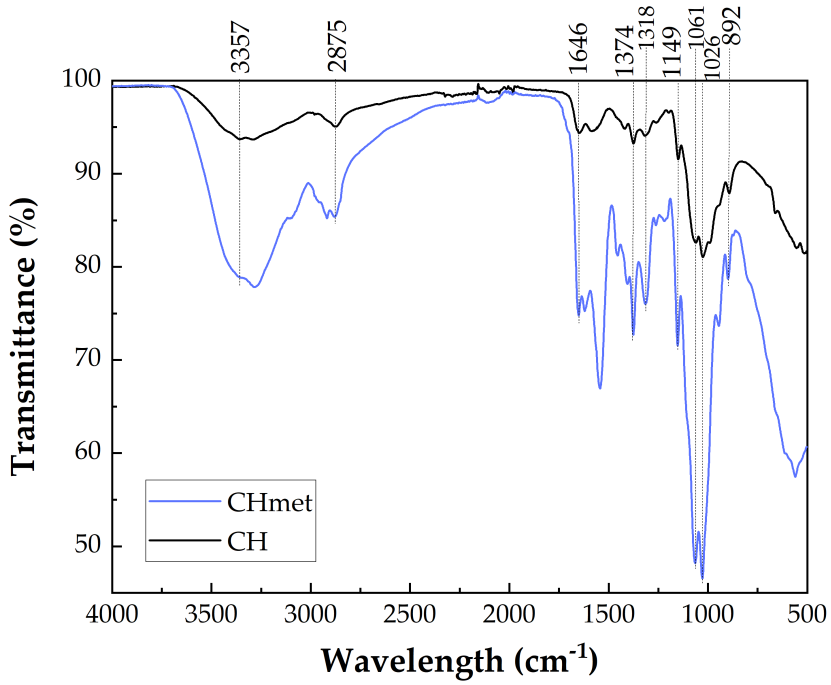


Figure 3-2 - FTIR-ATR spectra of chitosan (black line) and methacrylate chitosan (blue line). The common bands, the typical bands of chitosan, are connected and identified.

Clearly, in ChMA spectra, new characteristic bands can be identified. A zoomed-in view of ChMA spectra is presented in Figure 3-3, allowing the identification of a band at 3104 $cm^{-1}$,

typical of CONH group [44]. Subsequently, three new bands emerge at 2959 $cm^{-1}$, 2918 $cm^{-1}$, and 2850 $cm^{-1}$, attributed to the increased presence of methyl groups [43]. At 1621 $cm^{-1}$ it is possible to observe a band associated with the C-N of amide I from acetyl group [44] while at 1615 $cm^{-1}$, a band linked to C=C bond is evident [20]. Furthermore, the band at 1543 $cm^{-1}$ is due to the two amide N-H bonds [43] and the one at 1405 is associated with methyl groups [27]. Finally, at 801 $cm^{-1}$ the band correspondent to $C=CH_2$ is present [44]. All these new bands are related to the methacrylation process, attesting that chitosan was successfully methacrylated.

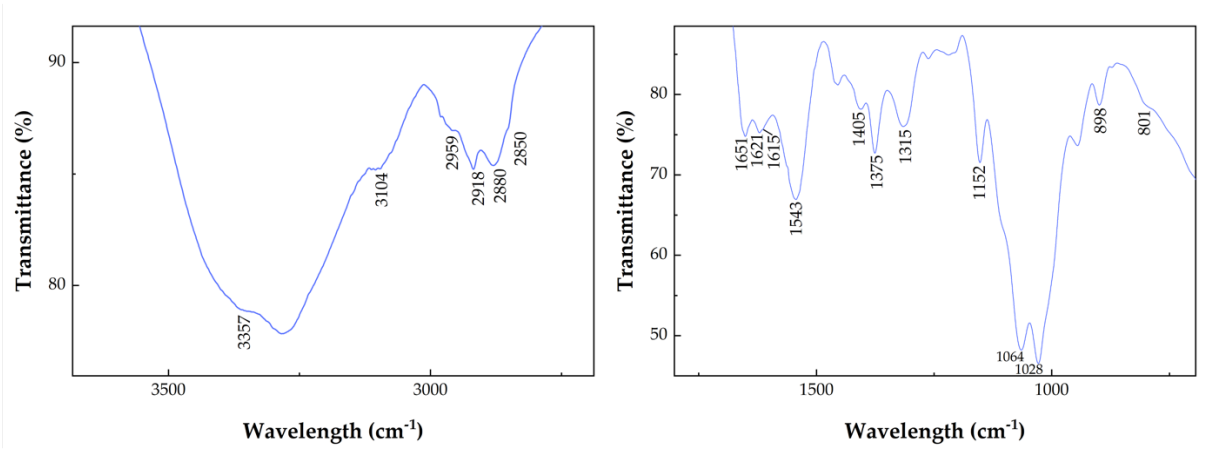


Figure 3-3 - FTIR-ATR of ChMA, divided in two zoomed-in images.

### 3.2.2 Scanning calorimetry with thermogravimetric analysis (DSC-TG)

TGA was performed to evaluate the thermal stability and degradation temperature of chitosan and ChMA. Figure 3-4A and B shows the TGA curves and their derivative, DTG, of chitosan and ChMA, respectively. Two distinct moments can be identified in the TGA curves of both polymers. The first moment occurs between 30 ºC and 120 ºC, in which the samples lose weight due to water loss [47][43]. In chitosan, the mass was reduced by 3.54% and in ChMA by 3.65%.

The next moment occurs between 270 ºC - 535 ºC for chitosan and 225 ºC - 535 ºC for ChMA, with an abrupt reduction in sample weight. This indicates the occurrence of pyrolysis in polysaccharides, which begins with the random breakage of glycosidic bonds and culminates with the production of acetic, butyric, and lower fatty acids [48]. At this stage, chitosan had a weight loss of 67.29% and a ChMA of 71.86%. The decomposition temperature of ChMA is 225 ºC, lower than chitosan's decomposition temperature of 270 ºC. Therefore, it is possible to conclude that ChMA has lower thermal stability than chitosan, as verified in [49]. At the end of the curves, it is possible to assess the residual weight of the samples, with ChMA having a residual weight of 32%, while chitosan had a higher value of 38.8%.

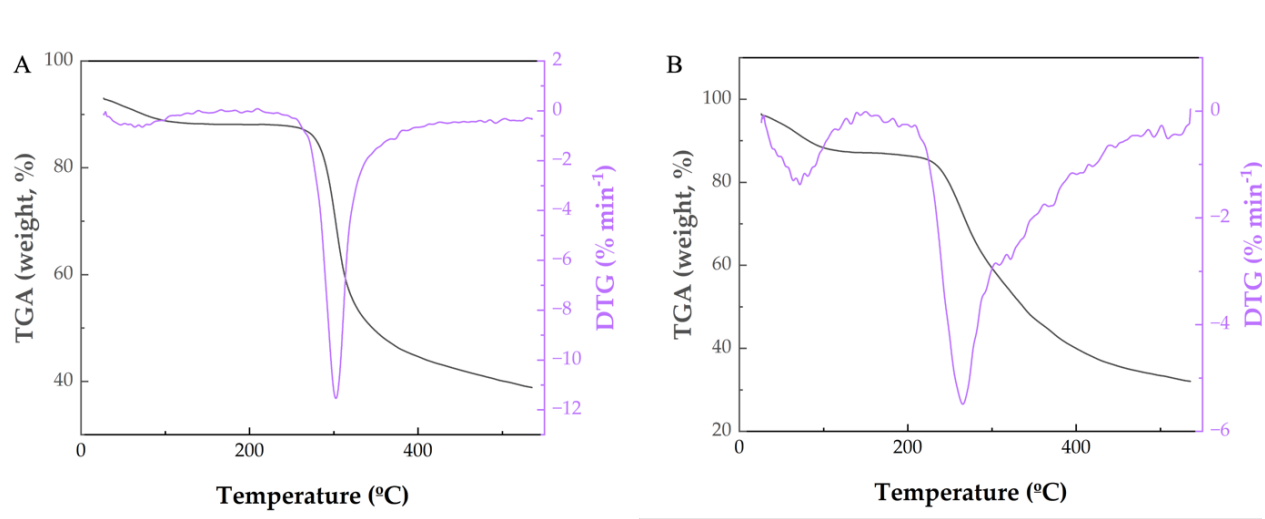


Figure 3-4 - A - TGA and DTG of chitosan. B - TGA and DTG of ChMA.

The chemical and thermal characterisation of ChMA allowed to conclude the methacrylation process was successful. In addition to these techniques, it would be appropriate to use the nuclear magnetic resonance ($^1$H-NMR) to confirm the methacrylation process and determine the methacrylation degree of the polymer. However, it was not possible to apply this technique within the timeframe of this work.

## 3.3 SPIONs production

In order to determine the concentration of nanoparticles in the obtained SPIONs suspension, the method described by Soares *et al*. [29] was followed. Using Equation 1

$$Abs = 3.5228[Fe] + 0.0583 \quad \text{(Equation 1)}$$

With Abs representing the average of the 5 samples absorbance and [Fe] the iron concentration, was applied to obtain the iron concentration. This equation is an updated version of the one used in the referenced work. A concentration of 24.60 mg mL$^{-1}$ was obtained. Next, the nanoparticle concentration was obtained through Equation 2

$$[Fe] = 0.7[NP] \quad \text{(Equation 2)}$$

In which [NP] represents the concentration of nanoparticles. The achieved value was 35.14 mg mL$^{-1}$.

## 3.4 Bioink Formulation

To develop different bioink formulations, the dissolution of the obtained polymer was first studied. Due to the difficulty of dissolving the polymer exclusively in water, a solution of 1.5% (w/w) of ChMA was made using a 0.5% (w/w) acetic acid solution, inspired by the protocol followed by Sayyar *et al*. [43]. However, after stirring overnight, the solution was not homogeneous.

Aiming to calculate the required acetic acid concentration to dissolute ChMA, the amount added to the mixture was gradually increased to 2% (w/w). It was still possible to observe some particles in the solution, even after 3 days of stirring. Therefore, the acetic acid concentration was increased to 3% (w/w), which allowed total and faster dissolution overnight. This increased difficulty in dissolution is not in accordance with [43], which can happen due to the lower degree of substitution of the obtained ChMA, which would lead to non-functionalized chitosan in the solution. Since chitosan requires acidic environments to dissolve, an increased acetic acid concentration to dissolve the polymer would be expected, as mentioned in [50].

## 3.5 Rheological assessment

The viscosity of each formulated bioink was evaluated since it must have enough viscosity to form a continuous filament and hold the bioprinted structure but not be too viscous that it clogs the nozzle. Besides that, this study also aimed to evaluate the influence of CNC concentration on the flow behaviour of the bioinks. The results are illustrated in Figure 3-5. Firstly, by the analysis of the viscosity curves, it is possible to conclude that all formulations containing CNC present shear thinning behaviour; this is, as the shear rate increases the viscosity decreases. This is positive for extrusion-based 3D bioprinting, as mentioned in the Theoretical concepts section, since the bioink suffers higher shear rate when extruded from the nozzle, leading to a lower viscosity which aids extrusion. When the bioink is deposited in the printing plate, suffers lower shear rate which leads to increased viscosity [34]. This behaviour is not observed for the solutions of ChMA, where an almost constant viscosity is obtained for all shear rates, approaching the behaviour of an idealized Newtonian fluid. In Table 2 the flow behaviour at lower and higher shear rates of the different formulations is displayed. The results showed that viscosity can be tuned by means of increasing ChMA and CNC content.

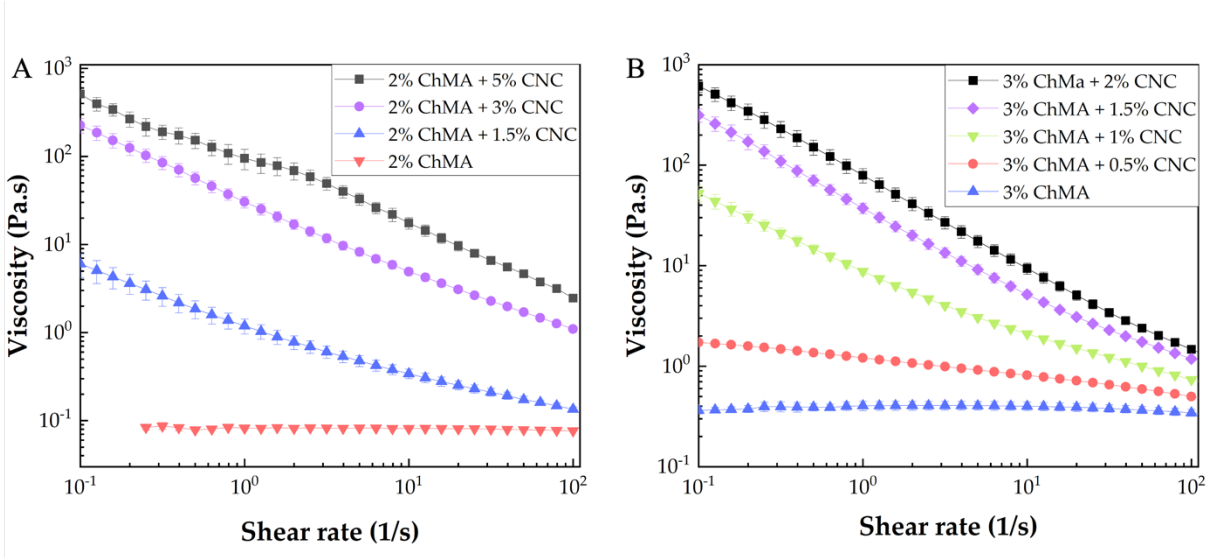


Figure 3-5 – Viscosity curves in function of shear rate of A – the bioinks with 2% ChMA; B – the bioinks with 3% ChMA.

Starting with the analysis of the control bioinks, it is possible to conclude that higher concentrations of ChMA lead to higher viscosities. This conclusion is supported by Shen *et al.* [38], although the flow behaviour values obtained in this study are superior to those obtained in the study by Shen *et al.*, for the same concentrations.

Table 2 – Viscosity values at lower and higher shear rates of each formulation

| **Formulation** | **Viscosity at lower shear rates (Pa.s)** | **Viscosity at 100 $s^{-1}$ (Pa.s)** |
|---|---|---|
| 2% ChMA | 0.08 | 0.08 |
| 2% ChMA + 1.5% CNC | 6.17 | 0.13 |
| 2% ChMA + 3% CNC | 224.76 | 1.01 |
| 2% ChMA + 5% CNC | 504.67 | 2.48 |
| 3% ChMA | 0.37 | 0.34 |
| 3% ChMA + 0.5% CNC | 1.70 | 0.50 |
| 3% ChMA + 1% CNC | 52.60 | 0.73 |
| 3% ChMA + 1.5% CNC | 314.38 | 1.17 |
| 3% ChMA + 2% CNC | 606.29 | 1.46 |

Regarding the formulations containing CNC, through the analysis of the values shown in Table 2 and the graphs displayed in Figure 3-5, it is possible to deduce that CNC actuates as a viscosity enhancer in bioinks, with higher CNC content leading to higher viscosities. This conclusion is in accordance with the literature, as verified by Maturavongsadit *et al.* [37], with chitosan bioinks reinforced with CNC. Besides that, in the work of Patel *et al*. [24], the enhancement of the flow behaviour of ChMA with the increasing addition of nanocellulose was also verified. Higher values for viscosity were obtained in this work, however a direct comparison is difficult since the authors used a different formulation, this is, higher content of ChMA, a different type of nanocellulose (spherical nanocellulose) and β-glucan.

## 3.6 3D bioprinting

The bioinks were chosen considering the viscosity and the appearance of the formulated mixture: an adequate bioink should not be too viscous, which can lead to aggregates and nozzle clogging, but should not be too fluid or else it will not offer suitable structural support to maintain the bioprinted shape without deformation. So, the bioink with 5% (w/w) CNC was excluded since with time tend to present to aggregates. Therefore, printing tests were performed with two formulations, 3% (w/w) of ChMA with 2% (w/w) of CNC, and 2% (w/w) of ChMA with 3% (w/w) of CNC. The printability of bioinks was assessed on the bioprinter by extruding a small amount and verifying the formation of a continuous and fluid extrusion for both bioinks, as described in [34], indicating good printability.

Various printing parameters were changed during the 3D bioprinting process to find the optimal printing conditions for this system. These parameters include printing flow, number of layers of the structure, printing velocity, nozzle size and layer height.

### 3.6.1 Preliminary 3D bioprinting of the bioink 3% (w/w) of ChMA with 2% (w/w) of CNC

First, the 3% (w/w) of ChMA with 2% (w/w) of CNC bioink without photocrosslinking was tested to assess the behaviour of the bioinks in these conditions. The first 3D bioprinted design was a straight line. The applied printing parameters were:

- Printing flows of 20% and 200%.
- The number of layers varied between 3 and 5 for each printing flow.
- A printing velocity of 0.5 mm $s^{-1}$, the minimum available on the bioprinter, was employed, taking into consideration future bioprinting involving simultaneous photocrosslinking, where sufficient time for layer crosslinking is imperative [51]. A decreased velocity leads to a longer printing time, allowing the photocrosslinking process to occur.
- Nozzle with a size of 22 G, similar to the one used in other 3D bioprinting works [24][40]

By analysis of Figure 3-6, it is possible to observe that the increase in printing flow led to increased thickness of the structures, as shown in Figure 3-6B, D and G. It is also possible to conclude that the flow of 20% is too low for this bioink due to the accumulation points visible in the structures represented in Figure 3-6A, C and E. The variation in the number of layers revealed a thickening effect on the bioprinted structure, similar to flow: more layers lead to thicker structures. Besides that, it is possible to observe that the structures' height is not uniform, forming ramp-shaped deformations on the edges. The best parameter in this case, which decreased these deformations, is the printing flow of 200% despite the number of layers, which effect is not as visible in the structures (Figure 3-6B and F). Further bibliographic research revealed that the observed deformations in the bioprinted structures occurred due to the lack of support of the lower layers to the rest of the structure since they did not stabilize, which implies they did not cease flowing after deposition [34]. This caused bioink dragging during the bioprinting process, accumulating in the structure's centre. Schwab *et al.* [34] presented two viable approaches for this situation: using bioinks with enough viscosity to support the structure or crosslinking during the bioprinting process to enhance the stabilization of the layers. So, it was opted to take the second approach.

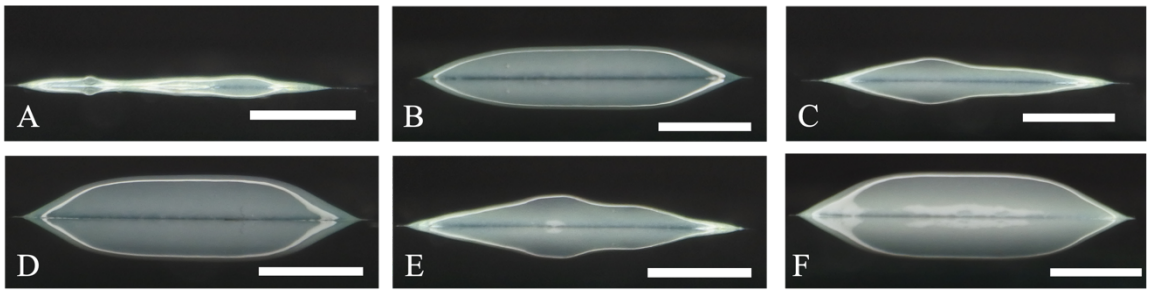


Figure 3-6 - Side view of the 3D bioprinted structures of the 3% ChMA with 2% CNC, formulation without Irgacure 2959. The printing velocity was 0.5 mm $s^{-1}$, the layer's height was 0.2 mm, and the 22 G nozzle was used. A– printing flow of 20% and 3 layers. B – printing flow of 200%, 3 layers; C - printing flow of 20%, 4 layers; D – printing flow of 200%, 4 layers; E – printing flow of 20%, 5 layers; F – printing flow of 200%, 5 layers. Scale bar: 2 mm.

### 3.6.2 3D bioprinting of the bioink 3% (w/w) of ChMA with 2% (w/w) of CNC with photocrosslinking during and after the bioprinting process

In this approach, the effect of photocrosslinking during and after the 3D bioprinting process on the structures was studied, aiming to reduce the "ramp" deformations previously observed.

Due to the previously observed results, a printing flow of 200% was used to bioprint a 5-layered structure, one of the combinations that minimizes the "ramp" deformation. A wider nozzle of 20 G was used to avoid the verified clogging of the end of the 22 G nozzle exposed to light, and the 0.5 mm $s^{-1}$ printing velocity was maintained. The bioprinting process took 5 minutes and 29 seconds and occurred under UV light. After this time, it could be observed that the structure was not completely crosslinked, so an additional UV light exposure was required. Before photocrosslinking occurred, the hydrogels dried, possibly due to the heat generated by the UV lamp and a reduction in the structure thickness was observed.

To avoid premature structure drying, a new attempt was made with different printing parameters:

- An 8-layered structure was bioprinted since it was previously verified that increasing the number of layers increases the structure's thickness.
- The printing flow was decreased to 100% due to the increased number of layers to maintain the structural integrity of the structure.
- The printing velocity remained 0.5 mm $s^{-1}$ as well as the nozzle of 20 G.
- The printing process took 8 minutes and 17 seconds, with UV light exposure, and an additional 15 minutes of UV light exposure was required.

Although it was possible to bioprint and photocrosslink hydrogels, the previously observed "ramp" deformations were substituted by dried regions in the edges of the hydrogels and photocrosslinked accumulation zones in the centre. This is illustrated in Figure 3-7A. To avoid this effect, new adjustments to printing parameters were performed:

- Layer height increased from 0.2 mm in Figure 3-7A to 0.4 mm in Figure 3-7B and 0.6 mm in Figure 3-7C to increase the thickness of the layers and, subsequently, the thickness of the edges.
- Printing velocity was increased to 1 mm $s^{-1}$ to avoid drying the lower layers through a shorter UV light exposure before the deposition of the next layers. This also aimed to increase the thickness of the edges.

A slight elongation of the crosslinked zone occurred with the higher layer height, as can be seen in Figure 3-7C. The same slight elongation is verified in Figure 3-7D, with the increased printing velocity. These results allow one to conclude that a higher printing speed and layer height are beneficial for the bioprinting process. However, the dry parts on the edges are still a major problem since they decrease the shape fidelity of the structure [47].

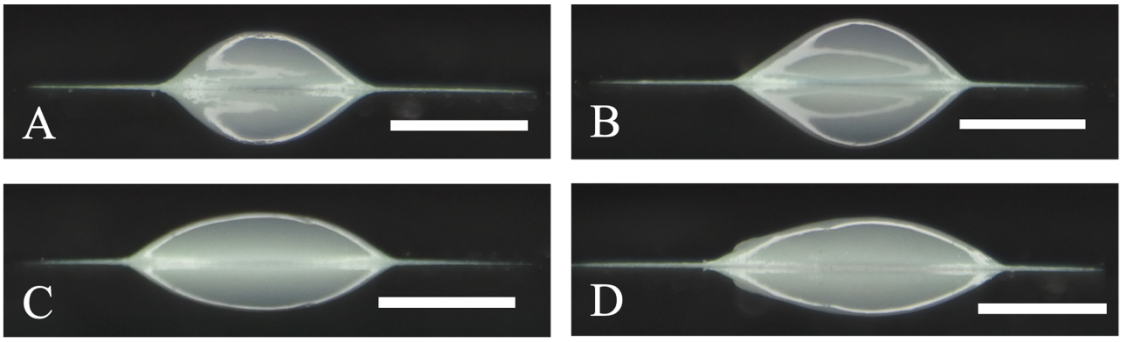


Figure 3-7 - Side view of 3D bioprinted hydrogels of 3% ChMA and 2% CNC, with UV light exposure of 8 minutes and 17 seconds during bioprinting and 15 minutes after bioprinting. A fixed printing flow of 100% and 20 G nozzle were used, as well as a fixed number of layers of 8. A – layer height of 0.2 mm and printing velocity of 0.5 mm $s^{-1}$. B – layer height of 0.4 mm and printing velocity of 0.5 mm $s^{-1}$. C – layer height of 0.6 mm and printing velocity of 0.5 mm $s^{-1}$. D - layer height of 0.2 mm and printing velocity of 1 mm $s^{-1}$. Scale bar: 2 mm.

A different design was bioprinted following this protocol, using the 3D model presented in Figure 4-2 of Annex A.3. The frame design was implemented to enable the evaluation of an additional aspect concerning shape fidelity within a single structure: assessing the geometry of the pores formed within the inner region of the frame [34].The printing parameters applied include:

- Variable printing flow of 10%, 20%, and 100% to assess the best values for this design.
- Contrary to the previous conclusions, the printing velocity was maintained at 0.5 mm $s^{-1}$ for a longer printing process to promote the photocrosslinking of the layers, as mentioned in [51].
- The number of layers was maintained at 8, as well as the 20 G nozzle.
- Despite the previous improvements with the increase in layer height, it was kept at 0.2 mm since this was the recommended layer height in the printing software.

- The bioprinting process took 10 minutes and 54 seconds, with simultaneous UV light exposure, and an additional 15 minutes of UV light exposure was required.

Through the observation of Figure 3-8A and B, it is possible to see their increased geometric accuracy when compared to Figure 3-8C. Between 10% and 20%, however, the difference is minimal. In conclusion, in this attempt, the lower flows showed better outcomes, contrary to the previously observed in the last design. The dried zones remained in this design, rounding the outer corners of the structure. The inner corners have a rounded shape as well.

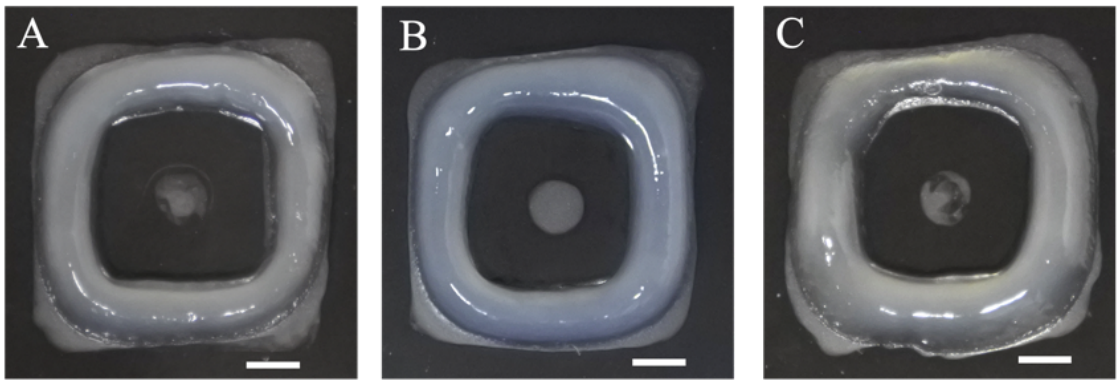


Figure 3-8 - Top view of 3D bioprinted frame structures of 3% ChMA with 2% CNC hydrogels with Irgacure 2959, with photocrosslinking during (10 minutes and 54 seconds) and after (15 minutes) the bioprinting process. A printing velocity of 0.5 mm $s^{-1}$, 0.2 mm of layer height, and 20 G nozzle were used, as well as a fixed number of layers of 8. A – printing flow of 10%; B – printing flow of 20%; C – printing flow of 100%. Scale bar: 2 mm.

Aiming to reduce the dried regions, the same protocol was followed with a change: to start the exposure to UV light later in the bioprinting process, this is, in the deposition of the third layer. This approach was a second attempt to reduce the exposure time of the lower layers, the most exposed to UV light regions, as mentioned above. These hydrogels were compared to hydrogels only exposed to UV light after bioprinting. The applied printing parameters were the following:

- Two printing flows were tested, 50% and 100%.
- The printing velocity remained 0.5 mm $s^{-1}$.
- The layers of the structure were increased to 12 to assess the effect of more layers in this design.
- The nozzle remained the same, 20 G, and the layer height 0.2 mm.
- The UV light exposure during bioprinting took 16 minutes and 15 seconds, and after bioprinting 15 minutes were necessary.

Through the observation of Figure 3-9, thicker structures highly deviated from frames were obtained. The difference between the hydrogels with UV light exposure exclusively after bioprinting and UV light exposure during and after bioprinting is minimal. The higher printing flow led to a thicker structure, supporting the previous conclusions. Between the two flows, as previously concluded, the best one is the lower, 50%. The increased number of layers resulted in hydrogels with visible structural collapse. The dried edges remained.

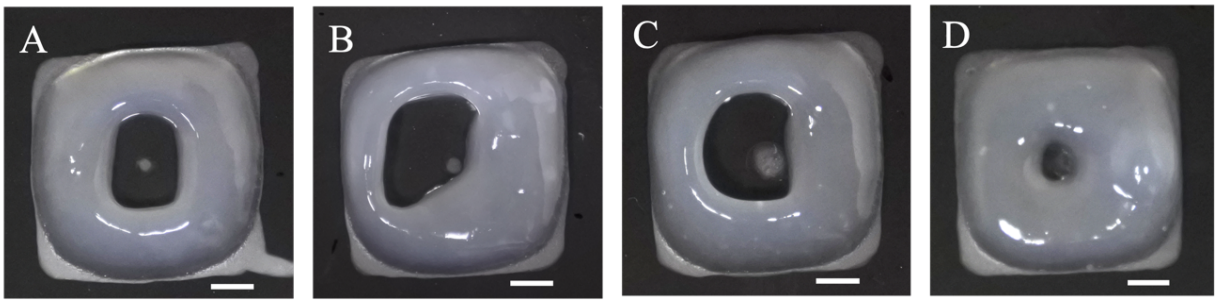


Figure 3-9 - Top view of 3% ChMA with 2% CNC hydrogels with Irgacure 2959. A printing velocity of 0.5 mm $s^{-1}$, 0.2 mm of layer height, and a 20 G nozzle were used, as well as a fixed number of layers of 12. A – printing flow of 100%, only post-bioprinting UV light exposure (15 minutes). B – printing flow of 100%, UV light exposure during (16 minutes and 15 seconds) and post-bioprinting (15 minutes). C – printing flow of 50%, only post-bioprinting UV light exposure (15 minutes). D – printing flow of 50%, UV light exposure during (16 minutes and 15 seconds) and post-bioprinting (15 minutes). Scale bar: 2 mm.

Lastly, the effect of the reduction on the nozzle size was assessed, carefully isolated with black opaque tape, to avoid clogging. In terms of printing parameters:

- Due to the conclusions mentioned above, the lowest flow possible was applied, 30%, higher than the used in Figure 3A due to the nozzle's decreased size.
- The printing velocity remained low, at 0.5 mm $s^{-1}$, to allow the photocrosslinking of the layers [51].
- The number of layers of the structure is 8, since increasing its number was shown not to be viable.
- The layer height remained the lowest, at 0.2 mm, since it is recommended by the printing software.
- The 22 G nozzle was tested.
- The bioprinting process took 10 minutes and 54 seconds, with UV light exposure, and an additional 15 minutes of UV light exposure was required.

The results are illustrated in Figure 3-10. A structure with thinner side widths was obtained. The rounded corners are slightly improved. In general, the geometric accuracy of the structure shows slight improvements when compared to the one obtained in Figure 3-8A and B, the better results obtained until this point. This shows that the 22 G nozzle can lead to better results than the 20 G nozzle.

After all these attempts, the problems presented before photocrosslinking during and after bioprinting still existed: the dried-out regions due to the thinner zones created in the structure because of bioink dragging coupled with high UV exposure time; the structural collapse because of the poor stability offered by the lower layers, leading to rounded corners. Further research allowed us to conclude that the remanence of these effects is due to the slow photocrosslinking process, which did not allow photocrosslinking and subsequent stabilization of the layers during the 3D bioprinting process, even with the lower printing speed. Therefore, the efficacy of UV exposure during bioprinting was low [34]. This is supported by the fact that all structures, with or without UV light exposure during bioprinting, required 15 minutes of

post-bioprinting exposure to photocrosslink. Manipulating the bioprinting process was not enough to solve the problem.

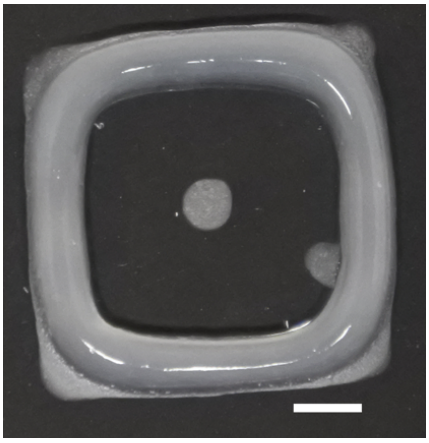

Figure 3-10 - Top view of a 3D bioprinted hydrogel from 3% ChMA with 2% CNC with Irgacure 2959 photocrosslinking during (10 minutes and 54 seconds) and after (15 minutes) the bioprinting process, printing flow 30%, printing velocity of 0.5 mm $s^{-1}$, 8 layers with layer height of 0.2 mm, bioprinted with a 22 G nozzle. Scale bar: 2mm.

The results obtained are not consistent with previously developed work in this area, in which complementary crosslinking methods and higher UV light intensity are frequently used, avoiding the effects of slower photocrosslinking processes in the bioprinted structures – which is not applied in this work until this point. Looking at concrete examples, in the work of Patel *et al*. [24], the developed 3D bioprinted ChMA hydrogels with β-glucan, spherical nanocellulose and LAP as the photoinitiator did not present any dried zones after the photocrosslinking process. In the bioprinted structures, however, it is possible to observe rounded corners, typical of filament collapse, like the obtained hydrogels in this work. In the 3D bioprinted ChMA hydrogels with β-glycerol phosphate and LAP developed by Tonda-Turo *et al*. [40], dried zones did not exist as well, after the photocrosslinking process. However, it is not possible to establish a direct comparison regarding the shape fidelity due to the different formulations of the bioinks used in these works and the fact that a pre-bioprinting crosslinking method was applied, especially considering the different types of crosslinking used. The lack of dried zones but the presence of rounded pores was also verified in the 3D bioprinted ChMA, methacrylate gelatine, hydroxyapatite and Irgacure 1173 hydrogels produced by Osi *et al*. [39]. A direct comparison of the crosslinking time and shape fidelity with the obtained hydrogels is not possible since different formulations and a complementary crosslinking method were applied besides photocrosslinking.

### 3.6.3 3D bioprinting of the bioink 3% (w/w) of ChMA with 2% (w/w) of CNC with pre-bioprinting photocrosslinking

As previously mentioned, Schwab *et al.* [34] presented two methods to decrease the observed deformations: crosslinking during bioprinting and bioinks with increased viscosity. The second approach was explored due to the unsuccessful application of the first one.

To achieve an increased viscosity, a method of photocrosslinking pre-bioprinting was applied, inspired by the method followed by Tonda-Turo *et al*. [40]. As a first attempt, the bioink was placed in a flask and exposed to UV light. Notably, 2 mL of bioink were crosslinked in 2 minutes, very different from the 15 minutes required to photocrosslink the bioprinted structures with a much smaller bioink volume. This observation will be explored further in this section.

Pre-bioprinting photocrosslinking of 30, 35, 43, and 45 seconds in a flask with subsequent transference to a syringe was tested. At 45 seconds, the hydrogel presented several aggregates, so bioprinting was not possible. The printing parameters were the same as applied to the last presented hydrogel:

- Printing flow 30% coupled with the 22 G nozzle, due to the better shape fidelity obtained in the last structure.
- Printing velocity remained 0.5 mm $s^{-1}$, 8-layered structures with a layer height of 0.2 mm.
- The bioprinting process took 10 minutes and 54 seconds, with UV light exposure, and an additional 15 minutes of UV light exposure was required.

The results of this approach, presented in Figure 3-11, present the same dried edges and rounded pores of the hydrogel in Figure 3-10. No improvements were verified, and therefore this approach was abandoned.

As previously mentioned, when exposed to UV light inside a flask, this mixture exhibited a photocrosslinking time much lower than required to photocrosslink the 3D bioprinted structures. To understand this event, deeper research on methacrylate chitosan and Irgacure 2959 reaction mechanism details was conducted. This brought to light that chain growth polymerization, the mechanism used to photocrosslink the hydrogels, explained in the section Theoretical concepts, is inhibited by oxygen [23]. This explains why the hydrogel crosslinks so much faster in a container in which air exposure is limited.

To achieve the desired photocrosslinking and stabilization of the lower layers of the structure during 3D bioprinting, leading to a reduction in dried regions and better shape of the hydrogels, decreasing the crosslinking time is crucial [34]. Two approaches were considered to solve this problem: the removal of oxygen or limitation of exposure to it during the crosslinking process, which is difficult due to the bioprinting process; switching the crosslinking reaction mechanism to step growth photopolymerization, which is not inhibited by oxygen, by the addition of thiol groups to the reaction [23]. This reaction mechanism is explained in the section Theoretical concepts.

### 3.6.4 3D bioprinting of the bioink 2% (w/w) of ChMA 3% (w/w) of CNC with photocrosslinking during and after the bioprinting process, with thiol groups

Dithiothreitol (DTT) was added to the mixture of 2% ChMA + 3% CNC, to include thiol groups in the reaction inserting step growth polymerization in the system, not dependent on the

oxygen presence [23]. This aimed to decrease the photocrosslinking time, as previously mentioned. The protocol followed to add this compound to the mixture was based on the procedure described in [23]. DTT was added to the mixture in a ratio of 1:5, as described in [23], to Irgacure 2959 and manually stirred for 20 minutes to ensure the fastest dissolution of the compound. It was left to degas in the fridge overnight.

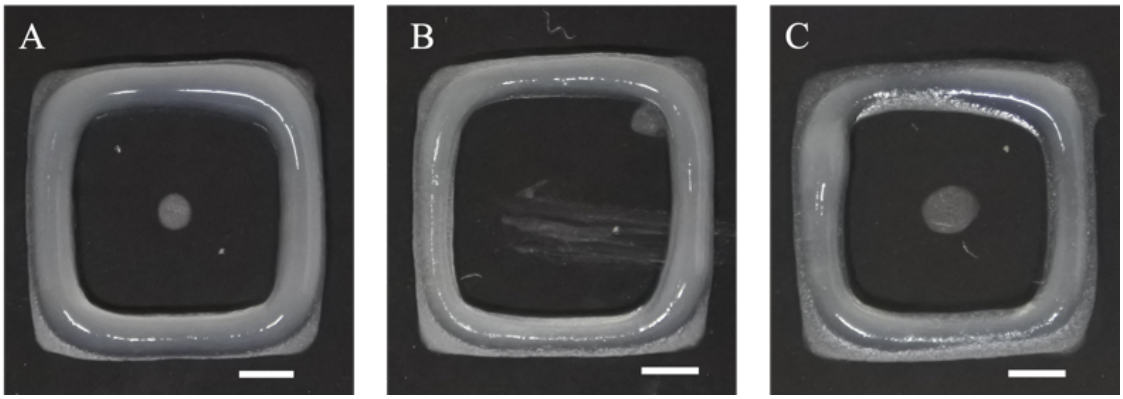


Figure 3-11 - Top view of 3% ChMA with 2% CNC hydrogels with Irgacure 2959 with photocrosslinking during (10 minutes and 54 seconds) and after (15 minutes) the bioprinting process, printing flow of 30%, printing velocity of 0.5 mm $s^{-1}$, 8 layers of 0.2 mm, bioprinted with 22 G nozzle. A – pre-bioprinting photocrosslinking of 35 seconds in a flask. B – pre-bioprinting photocrosslinking of 40 seconds in a flask. C – pre-bioprinting photocrosslinking of 43 seconds in a flask. Scale bar: 2 mm.

First, to determine if the oxygen exposure affected the photocrosslinking time, two structures were 3D bioprinted with two different printing velocities, attempting to decrease oxygen exposure and UV light exposure only after bioprinting. In both structures, the crosslinking time successfully decreased to 2 minutes and 30 seconds, showing that the printing speed used did not have a relevant role in this process.

The efficacy of photocrosslinking during bioprinting was assessed. The printing parameters were the following:

- The printing flow was 100%, a pre-determined suitable flow for the new formulation.
- Since the printing velocity did not affect the post-bioprinting photocrosslinking time, 2 mm $s^{-1}$ was chosen, as a balance between printing duration and printing speed to allow the photocrosslinking of the structure. Due to the reduction of the photocrosslinking time, a faster bioprinting process could be applied [51].
- The nozzle of 22 G, layer height of 0.2 mm and 8 layers were maintained, since they were previously used in the best structure obtained, represented in Figure 3-10.
- The structure with only post-bioprinting UV exposure required 2 minutes and 30 seconds to photocrosslinking and the one with UV exposure during bioprinting (for 2 minutes and 53 seconds) required 2 additional minutes of post-crosslinking UV light exposure.

The results are illustrated in Figure 3-12. The hydrogel that underwent photocrosslinking during and after the bioprinting process, in Figure 3-12C and D, presents a decreased side width and higher and homogenous height compared to the hydrogel of Figure 3-12A and B, only photocrosslinking after bioprinting. The dried areas are substantially decreased in both hydrogels.

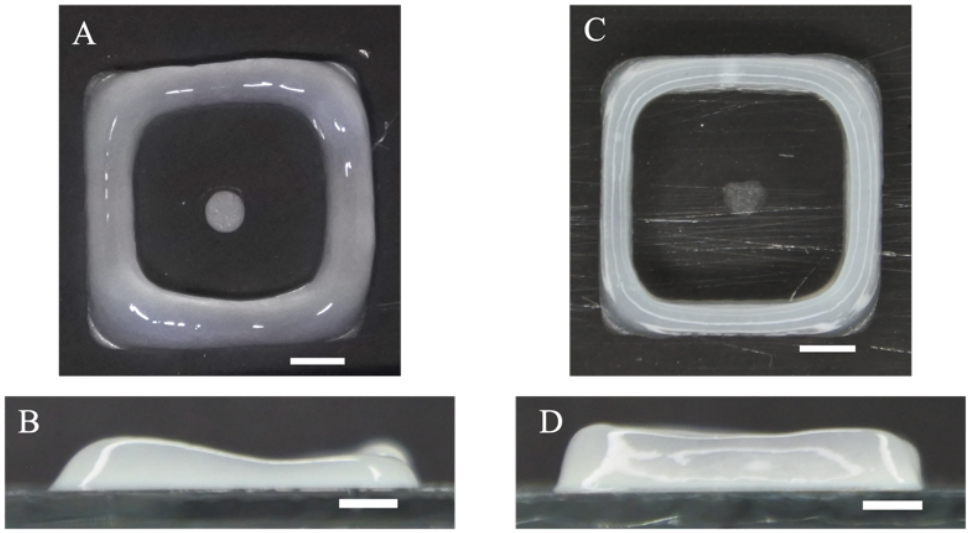


Figure 3-12 - 3D bioprinted hydrogels of 2% ChMA with 3% CNC, with printing flow of 100%, printing speed of 2 mm $s^{-1}$, 8 layers of height 0.2 mm and 22 G nozzle used. A, B – top and side view, respectively, of hydrogels with UV exposure only after bioprinting for 2 minutes and 30 seconds. C, D – top and side view, respectively, of hydrogels with UV exposure for 2 minutes and 53 seconds and after bioprinting of 2 minutes.

The width and height of the hydrogel that underwent photocrosslinking during the 3D bioprinting process reveal the lower spreading of the bioink and better layer stacking of the structure, respectively. These are signs of successful photocrosslinking of the layers during 3D bioprinting [34]. Besides that, photographs also showed that the dried regions are decreased as well.

When put in water, it was possible to see some hydrogel particles floating after washing. Although this formulation leads to an increased shape fidelity of the 3D bioprinted structures, the presence of CNCs might inhibit the crosslinking between the ChMA and Irgacure. This might reveal the low stability of the matrix of the hydrogels prepared from this formulation, probably due to the high CNC percentage when compared to ChMA. To prove this hypothesis, tests using the mixture featuring 3% ChMA with 2% CNC were also performed.

### 3.6.5 3D bioprinting of the bioink 3% (w/w) of ChMA with 2% (w/w) of CNC with photocrosslinking during and after the bioprinting process, with thiol groups

The same procedure was followed, and the same printing parameters were applied as described in the section above, with UV light exposure during and post-bioprinting. The photocrosslinking post-bioprinting time decreased to 1 minute and 30 seconds. After washing, the

number of particles in water was minimal compared with the last scenario, which might be a good indication that the problem was indeed due to the poor stability of the matrix. However, replicating this process was not possible due to the high sensibility of the mixture to the light, which made it impossible to bioprint the mixture because it underwent photocrosslinking inside the syringe, clogging it. These effects were not seen previously with the mixture of 2% ChMA with 3% CNC because, in 3% ChMA with 2% CNC, the higher percentage of ChMA, Irgacure 2959 and DTT led to more photoreactive groups in the solution. Therefore, the reaction rate increased, which is also shown by the above-mentioned decrease in photocrosslinking post-bioprinting time.

To solve this problem, and since the hydrogels of 2% ChMA with 3% CNC were not stable, the DTT amount was reduced to a ratio of 1:15 to Irgacure 2959 to decrease the reaction rate, lowing its sensibility to the UV light exposure. The same bioprinting preparation protocol was followed, with new precautions to avoid the previous events. All the processes of DTT addition and preparation of the syringe were performed in a dark room; a) before the bioprinting process, the syringe with the mixture was placed in the fridge for 30 minutes, to slow the crosslinking process caused by some residual light exposure; b) the placement of the syringe, isolated with black tape, in the bioprinter holder, was also made in the dark and this region was isolated with aluminium foil before exposure to the light required to perform the bioprinting. Besides that, the bioprinting process was performed as fast as possible, so the crosslinking process that could occur due to light reaching the syringe holder does not affect the bioprinting process. The printing parameters were:

- The printing flow was varied from 60% to 140% to assess the best value.
- The printing velocity was decreased to 1 mm $s^{-1}$, increasing the printing time to ensure the photocrosslinking of the layers with the lower reaction rate [34] [51].
- The nozzle 22 G, 8 layers and layer height of 0.2 mm were maintained, for the above-mentioned reasons.
- The printing took 5 minutes and 30 seconds with simultaneous UV exposure, and the post-bioprinting UV exposure took 2 minutes and 30 seconds.

By analysis of Figure 3-13A, B, C and D, it is possible to observe bioink accumulation points along the structure in hydrogels bioprinted with a printing flow of 60% and 80%. On the other hand, in Figure 3-13E to J, it is possible to observe the homogeneous height, reduced amount of dried zones and slightly rounded pores of the structures originated by printing flows 100%, 120% and 140%.

The obtained results allowed the exclusion of printing flows 60% and 80% in the choice of the best printing flow. Flows 100%, 120% and 140% present an improved geometric accuracy and lower collapse of the layers, showing the successful photocrosslinking and stabilization of the layers. The post-bioprinting photocrosslinking time was higher than the previous hydrogels due to the reduction in the reaction rate caused by the decreased DTT amount.

To assess the best printing flow among printing flows 100%, 120%, and 140%, the analysis of shape fidelity was made. The measures to assess the shape fidelity were obtained from the

bioprinted hydrogel photographs with the software Image J. The methods applied were a quantitative analysis inspired by Webb *et al*. [52], through a comparison of the measurements of the obtained hydrogels with the 3D model dimensions and methods described in [34], layer stacking and pore geometry.

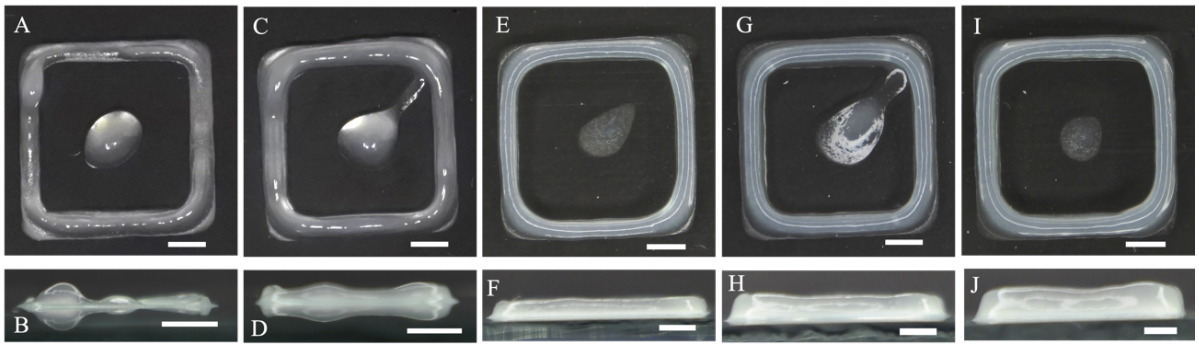


Figure 3-13 - 3D bioprinted 3% ChMA with 2% CNC hydrogels, with photocrosslinking during (5 minutes and 30 seconds) and after (2 minutes and 30 seconds) bioprinting, printing speed of 1 mm $s^{-1}$, 8 layers of height 0.2 mm and 22 G nozzle used. A, B – top view and side view, respectively, of printing flow 60%. C, D – top view and side view, respectively, of printing flow 80%. E, F – top view and side view, respectively, of printing flow 100%. G, H – top view and side view, respectively, of printing flow 120%. I, J – top view and side view, respectively, of printing flow 140%.

Measurements of the width (a, b, c, d in Figure 3-14), the total width of the hydrogel (e, indicated in Figure 3-14) and the hydrogel thickness were obtained from three replicas. These measurements, in the 3D model, are 0.600 mm for a, b, c and d; 10,0 mm for e and 1.64 mm for thickness. A 3D model preview is presented in Figure 4-2 of Annex A.2.

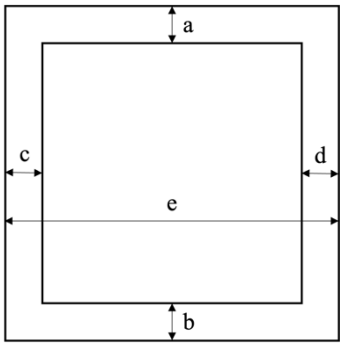


Figure 3-14 - Scheme of the performed measurements in the hydrogels to assess their shape fidelity.

Each measurement of the hydrogel was subtracted from the respective measure of the 3D model, obtaining their deviations, as observed in Equation 3:

$$Deviation = m_{3D\ printed\ structure} - m_{3D\ model} \qquad \text{(Equation 3)}$$

In which $m_{3D\ bioprinted\ structure}$ represents the measures performed in the 3D bioprinted structure and $m_{3D\ model}$ the respective measure in the 3D model. The average deviation of the three replicas was calculated for a, b, c, d,e and thickness. Using this value, the relative percentage error was calculated, according to the following equation:

$$Relative\ percentage\ error\ (\%) = \frac{Deviation\ average}{m_{3D\ model}} \times 100 \qquad \text{(Equation 4)}$$

In which $m_{3D\ model}$ represents the respective measure in the 3D model, as in the equation above. The results are presented in Table 3.

Positive deviation values mean that the bioprinted structures are larger than the 3D model in that measurement, as large as the deviation value. On the other hand, negative values mean that the structures are smaller than the 3D model, as smaller as the deviation value. The relative percentage error shows how different from the 3D model the measures obtained are in percentage. The bigger the value of the relative percentage error, the more different from the 3D model that measure is.

Table 3 - Measurements to assess shape fidelity.

| | **Printing flow 100%** | | | | | |
|---|---|---|---|---|---|---|
| | **a** | **b** | **c** | **d** | **e** | **Thickness** |
| **Deviation average (mm)** | 0.807 ± 0.418 | 0.823 ± 0.470 | 0.890 ± 0.502 | 0.607 ± 0.306 | 0.540 ± 0.390 | -0.982 ± 0.027 |
| **Relative percentage error (%)** | 134 | 137 | 148 | 101 | 5.40 | 59.9 |
| | **Printing flow 120%** | | | | | |
| | **a** | **b** | **c** | **d** | **e** | **Thickness** |
| **Deviation average (mm)** | 0.973 ± 0.486 | 0.890 ± 0.410 | 1.01 ± 0.523 | 0.823 ± 0.349 | 0.683 ± 0.527 | -0.954 ± 0.043 |
| **Relative percentage error (%)** | 162 | 148 | 169 | 137 | 6.83 | 58.3 |
| | **Printing flow 140%** | | | | | |
| | **a** | **b** | **c** | **d** | **e** | **Thickness** |
| **Deviation average (mm)** | 0.837 ± 0.295 | 0.923 ± 0.253 | 0.950 ± 0.289 | 0.797 ± 0.232 | 0.570 ± 0.161 | -0.865 ± 0.155 |
| **Relative percentage error (%)** | 139 | 154 | 158 | 133 | 5.70 | 52.7 |

Given these data and analysing the deviations, it is possible to conclude that all bioprinted structures presented wider sides than the 3D model (a, b, c, d in Figure 3-14) and larger structure width (e in Figure 3-14). On the other hand, the thickness of all hydrogels was smaller than the 3D model. This is a signal of poor layer stacking, indicating spreading to the lower layers [34], which leads to lower thickness and higher width.

Regarding relative percentage errors, it is possible to conclude that the lower values, that correspond to lower differences to the 3D model dimensions, are obtained from printing flow 100%, except in thickness, which has the higher value. However, for most measures, printing flow 100% presents the most approximate dimensions compared to the 3D model. This indicates the superior geometric precision of the structure, making it the most successful bioprinting [52]. Therefore, 100% was considered the best tested printing flow for this bioink, when coupled with the other printing parameters used: printing velocity of 1 mm $s^{-1}$, layer height 0.2 mm and nozzle of 22 G.

Besides the quantitative analysis, by analysing the pore shape, it is also possible to infer on the quality of the bioprinting process. The rounded corners of the pore support the conclusion that the collapsing of the lower layers was still observed, although reduced [34].

To better assess the shape fidelity of the best printing flow, a grid design was successfully bioprinted, with the printing parameters mentioned above. However, an increase in UV light exposure during bioprinting was necessary due to the higher printing time (8 minutes and 6 seconds). Results are presented in Figure 3-15. The above-mentioned rounded pores are obvious in the more intricate details of the grid, and irregular height is caused by the collapse of filaments [34].

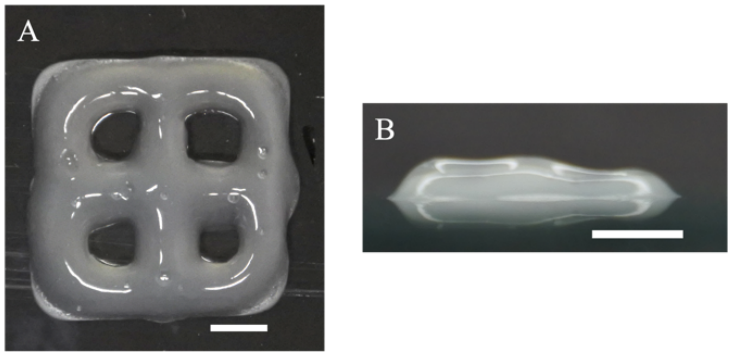


Figure 3-15 - 3D bioprinted grid-shaped 3% ChMA with 2% CNC hydrogel with photocrosslinking during (8 minutes and 6 seconds) and after (2 minutes and 30 seconds) bioprinting, printing flow 100% and printing velocity 1 mm $s^{-1}$, printing speed of 1 mm $s^{-1}$, 8 layers of height 0.2 mm and 22 G nozzle used. A – top view. B – side view.

Finally, the mixture of 3% ChMA with 2% CNC incorporating SPIONs was bioprinted, with the best printing flow and the same lastly described printing parameters:

- Printing flow of 100% and printing velocity of 1 mm $s^{-1}$.
- 8 layers and a layer height of 0.2 mm.
- The nozzle of 22 G.
- Printing duration of 5 minutes and 30 seconds for the frame design and 8 minutes and 6 seconds for the grid design with simultaneous UV exposure and the post-bioprinting UV exposure of 2 minutes and 30 seconds.

However, when exposed to UV light, these hydrogels were not photocrosslinked. The structures were exposed to 12 minutes of post-bioprinting UV light exposure. By the end of this

time, the structures were dried or if not completely dried, the remaining hydrated parts were not crosslinked, as one can observe in Figure 3-16A and B. Possible causes for this include the inhibition of the photocrosslinking reaction due to the concentration of SPIONs in the bioink, which may absorb the applied 365 nm UV light, as SPIONs have an absorbance peak at 400 nm [53]. Additionally, the inhibition of photocrosslinking may occur due to the bonding of the OH groups of SPIONs to ChMA. The negative impact of SPIONs on the crosslinking process of hydrogels was previously reported in the literature by Ko *et al.* [41]. They found that higher concentrations of SPIONs inhibited the crosslinking reaction between glycol chitosan and oxidized hyaluronate. The authors attributed this inhibition to the interference of the anionic nature of SPIONs in the reaction.
Besides that, another problem verified in the obtained structures was the aggregation of SPIONs, which can be observed in Figure 3-16C. However, this was the first attempt at incorporating SPIONs in this system and, within the time of this dissertation, could not be further developed.

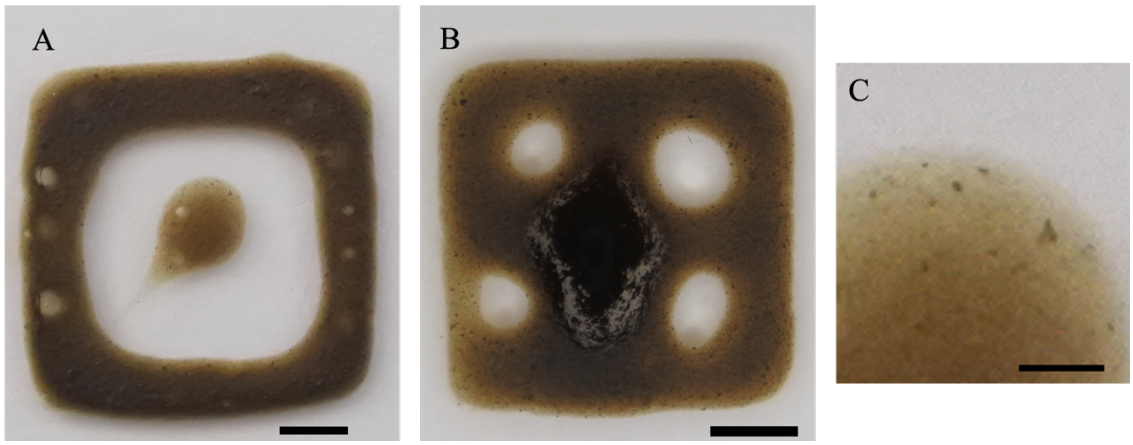


Figure 3-16 - 3D bioprinted hydrogels with 3% ChMA, 2% CNC and SPIONs, printing flow 100% and printing velocity 1 mm $s^{-1}$, 8 layers of height 0.2 mm and 22 G nozzle used. A – frame design, completely dried, with UV exposure during (5 minutes and 30 seconds) and after (12 minutes) bioprinting. B – grid design, with UV exposure during (8 minutes and 6 seconds) and after (12 minutes) bioprinting. It is possible to see the dried and fluid parts, which are not crosslinked. C – zoom-in of A. Scale bar: 2 mm for A and B; 0.5 mm for C.

## 3.7 Production of hydrogels using moulds

To characterise the system described in this master thesis, hydrogels were produced by using moulds, using the pre-determined better formulation for 3D bioprinting, 3% (w/w) ChMA with 2% (w/w) CNC, Irgacure 2959 and DTT. The photocrosslinking time of the hydrogels was increased to 5 minutes and 30 seconds, due to the higher volume of formulation used, in the preparation of each structure, compared with the 3D bioprinted structures.
The hydrogels without SPIONs were fully crosslinked and stable after the above-mentioned crosslinking time. However, as expected, due to the 3D bioprinting results, the hydrogels featuring SPIONs did not photocrosslink. Due to this problem, it was impossible to characterise the system featuring SPIONs in this master thesis.

## 3.8 Mechanical tests

The assessment of the mechanical properties of a hydrogel destined for 3D bioprinting is important since it must have enhanced strength to support the bioprinted structure. The mechanical properties of hydrogels made of the chosen formulation for 3D bioprinting were evaluated using a universal testing machine in compression mode. A stress/strain curve of one of the five samples evaluated is illustrated in Figure 3-17A. It is possible to observe a linear elastic region at low stresses, followed by a plastic deformation associated with plastic buckling collapse, characterised by the collapse of the structure's pores. Then, a sudden rise in the graph reveals a densification stage [54].
The compressive modulus was obtained by determining the slope of the linear elastic region. The application of this procedure for the presented curve is shown in Figure 3-17B.

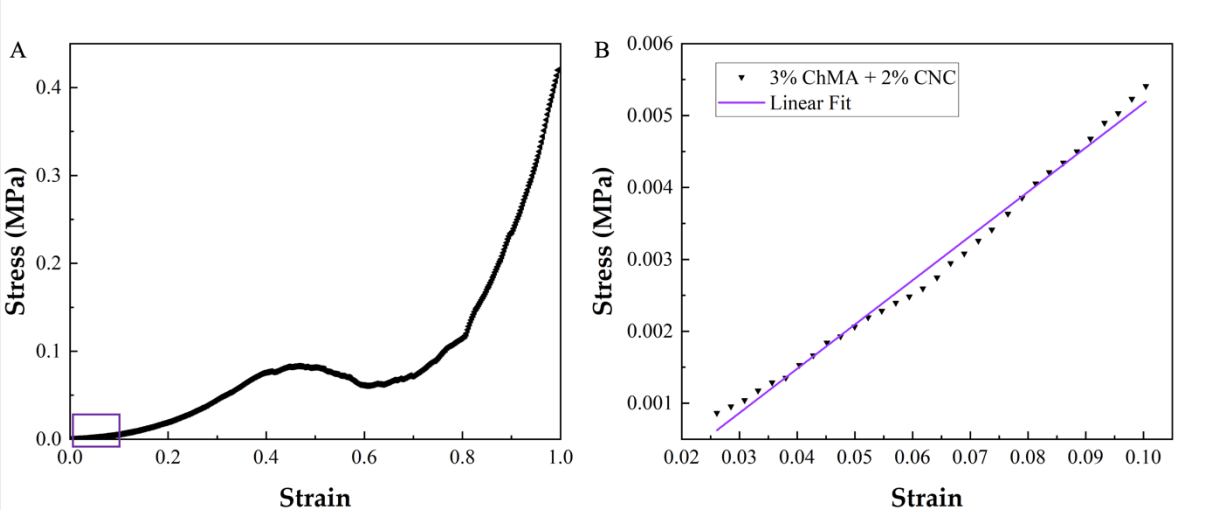


Figure 3-17 - Stress/strain curve of a hydrogel of 3% ChMA with 2% CNC, with Irgacure 2959 as the photoinitiator and DTT. The purple rectangle highlights the linear elastic region. B – The linear elastic region of graph A. A linear fit was applied to calculate its slope, which is the value of the compressive modulus.

The obtained value after the assessment of all samples was 70.82 ± 11.67 kPa. When compared with the compressive modulus reported in other studies within the field of 3D bioprinting, this value is relatively high, indicating good mechanical properties for this application [24] [39] [55]. Much lower values of compressive modulus were presented by Zhu *et al.* in [23] for hydrogels featuring 1.5% (w/w) ChMA with Irgacure 2959 and DTT, with the same reaction mechanism. In this study, the obtained hydrogels are reported to feature a compressive modulus below 10 kPa. It is possible to infer that this lower value relative to the obtained values in this study can be due to the lower ChMA concentration employed, as well as the lack of reinforcing agent CNC, already seen to improve mechanical properties when applied in chitosan hydrogels by Maturavongsadit *et al.*in [37]. Specifically, in this study, it was verified that in hydrogels containing 2% (w/w) chitosan, the compressive modulus increased from 85.12 Pa in chitosan-only bioinks to 122.12 Pa and 132.40 Pa in formulations with 0.5% (w/w) and 1.5% (w/w) CNC, respectively.

## 3.9 PBS absorption test

PBS absorption tests were carried out in freeze-dried hydrogels containing 3% ChMA and 2% CNC, together with Irgacure 2959 and DTT. The goal was to test the photocrosslinked hydrogels' ability to absorb and hold phosphate-buffered saline (PBS), which mimics physiological environment. To do this, the weight swelling ratio ($S_w$) was calculated using the Equation 5 [56]:

$$S_w = \frac{w_t - w_0}{w_0} \times 100 \qquad \text{(Equation 5)}$$

With the $w_t$ representing the weight of the hydrogel each time interval and $w_0$ the dried hydrogels weight. Seven samples were evaluated, and the result is illustrated in Figure 3-18.

By the analysis of the graph, it is possible to conclude that the higher PBS uptake, of 2493 ± 329 %, was verified after 5 hours. It is also worth noting that the swelling in hydrogels seems to be instantaneous, followed by a period of stabilization during the remainder of the test, where no further increase is observed, reaching the maximum PBS uptake. Comparing the obtained results with previous works, in the study conducted by Zhu *et al*., hydrogels with 1.5% (w/w) of ChMA, Irgacure 2959 and DTT with a $S_w$ of 2750% after 2 days of immersion were reported [23]. This value is close to the obtained in this study, with a slight reduction which can be associated with the presence of CNC.

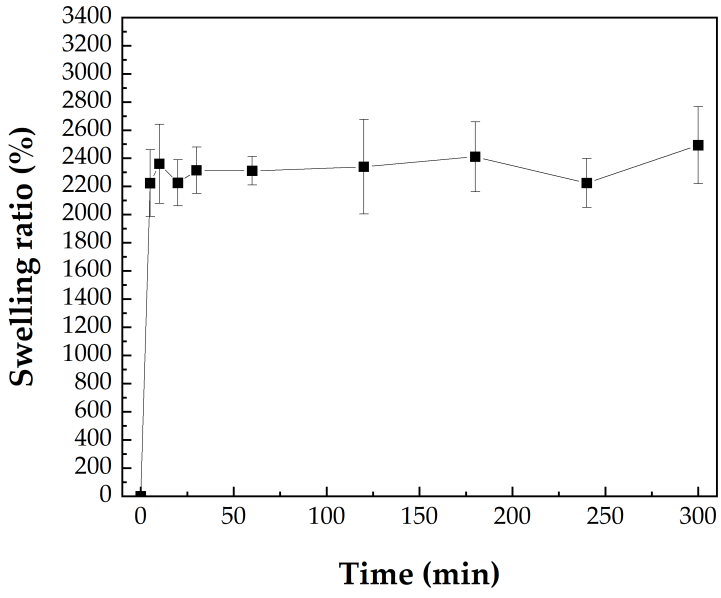


Figure 3-18 - Variations in the swelling ratio of hydrogels of 3% ChMA with 2% CNC, with Irgacure 2959 and DTT measure at specific time intervals during 5 hours in PBS (pH = 7.4).

## 3.10 Morphological analysis

Scanning electron microscopy (SEM) was the chosen technique to evaluate the microstructure of the hydrogels. Figure 3-19A illustrates a cross-section of the hydrogel, a close-up of the wall

of one of the pores can be found in Figure 3-19B and D, and the surface of the hydrogel in Figure 3-19C.

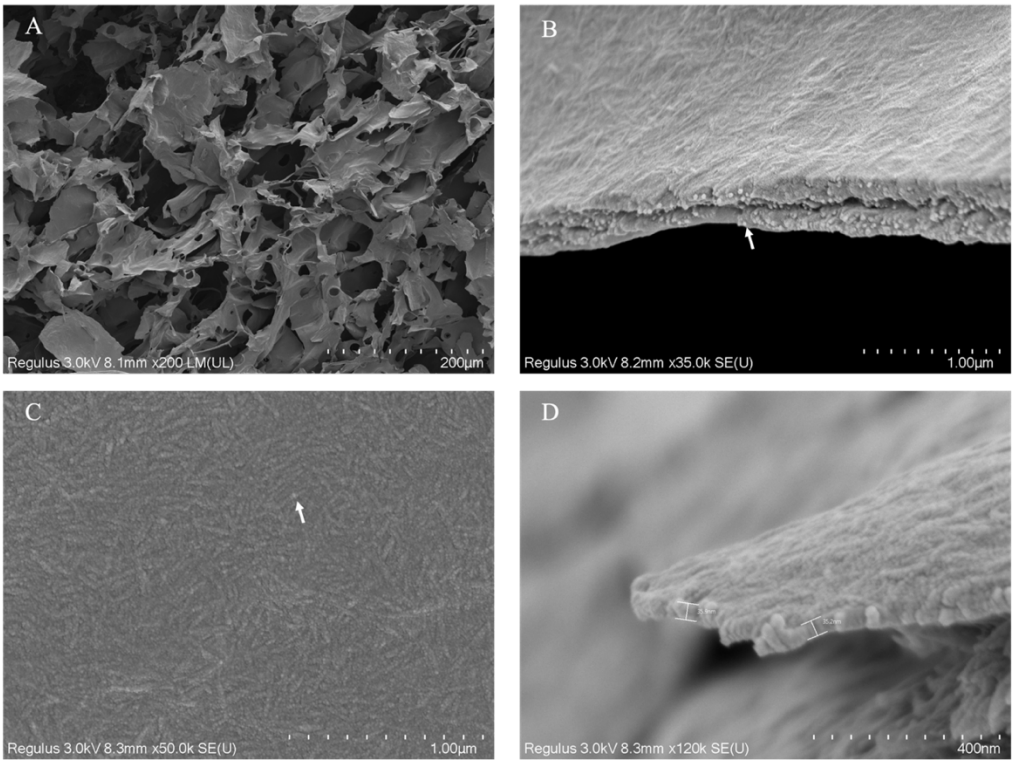


Figure 3-19 - SEM images of 3% ChMA with 2% CNC hydrogel, with Irgacure as the photoinitiator and DTT. A – cross-section of the hydrogel. B, D – close up of the wall of a pore, with CNC visible and signed with an arrow in B. C – Top view of the hydrogel, with CNC visible and signed with an arrow.

Analysing Figure 3-19A, one can observe the microstructure of the hydrogel, which shows the presence of irregularly shaped and sized porous. This is consistent with the work of Shen *et al*. [38], in which ChMA hydrogels were developed, and with the porous surface of the composite hydrogels composed of ChMA, spherical nanocellulose and β-glucan presented by Patel *et al*. [24]. A highly porous matrix is an advantage in hydrogels destined for drug delivery since it allows the transport and gradual release of the carried drug [9]. Besides that, in Figure 3-19B it is possible to observe the wall of a pore, providing the view of the fibrous content of the structure, pointed with an arrow. Regarding the pore walls, it is also clear in this image that they are made up of several planes stacked on each other. In Figure 3-19C, the CNC content can be observed on the surface of the hydrogel, appearing as small, brighter spherical particles indicated by an arrow in the image. The homogeneous dispersion of these particles is evident. Measurements of the thickness of a wall of a pore on Figure 3-19D returns a value around 30 nm, while Figure 3-19B show thicker walls.

# 4

# CONCLUSIONS AND FUTURE PERSPECTIVES

## 4.1 Conclusions

This master thesis aimed to develop a novel system of photocrosslinkable 3D bioprinted ChMA hydrogels, reinforced with CNC and using Irgacure 2959 as the photoinitiator, with SPIONs incorporated. In this subject several advances were made, in the study of bioink formulations to develop one suitable for 3D bioprinting and studying the printing parameters, manipulating the 3D bioprinting protocol and the photocrosslinking process to obtain 3D bioprinted hydrogels. Besides that, the first steps in characterising a non-documented system that combines ChMA, CNC, Irgacure 2959 and DTT in a hydrogel were made.

Through the observation of the obtained FTIR-ATR spectra, one can verify the successful methacrylation of the chitosan, due to the appearance of bands associated with chitosan and the methacrylation process. DSC-TG analysis allowed us to conclude that the degradation of ChMA with high temperatures occurs in a two-staged process similar to chitosan. However, the lower thermal stability of ChMA was verified due to its lower degradation temperature of 225 ºC when compared to the degradation temperature of chitosan, 270 ºC.

The rheological assessment of the bioink formulations was performed, showing that CNC actuates as viscosity enhancers in the bioinks. Besides that, it is also possible to conclude that the bioinks with higher viscosity at lower shear rates were 3% (w/w) ChMA with 2% (w/w) CNC, 2% (w/w) ChMA with 3% (w/w) CNC and 2% (w/w) ChMA with 5% (w/w) CNC with viscosities of 606.29 Pa.s, 224.76 Pa.s and 504.67 Pa.s, respectively. This supports the choice of bioinks for 3D bioprinting since the chosen bioinks are viscous to hold the structure shape but not too viscous that form aggregates, such as in the case of the formulation 2% (w/w) ChMA with 5% (w/w) CNC. This test also showed the shear thinning behaviour of all bioinks, appropriate for 3D bioprinting.

On the 3D bioprinting process, the two bioink formulations, 3% (w/w) ChMA with 2% (w/w) CNC and 2% (w/w) ChMA with 3% (w/w) CNC, both showed good printability due to their continuous extrusion. The 3D bioprinting of the 3% (w/w) ChMA with 2% (w/w) CNC bioink was tested first, without photocrosslinking during bioprinting, leading to a deformed shape. This allowed us to understand that the lower layers of the bioprinted structure did not provide enough support to the rest of the structure due to their lack of stabilization after extrusion. This led to bioink dragging during bioprinting, which deformed the structure. UV exposure was provided during bioprinting so the layers could photocrosslink, to increase their stabilization. However, the chain growth mechanism activated when ChMA and Irgacure 2959 are mixed and exposed to UV light is inhibited by oxygen, which makes the photocrosslinking process very slow. Therefore, it was concluded that the photocrosslinking during bioprinting was still not enough to stabilize the layers, leading to the same deformed structures. This deformation was enhanced by the required long UV exposure to photocrosslink the structures, which led to dried zones. Several unsuccessful attempts were made to reduce this effect by manipulating the printing parameters and exposure to UV light. A switch in the reaction mechanism was then tested in the bioink, 2% (w/w) ChMA with 3% (w/w) CNC, by adding DTT to the mixture, which activated the step growth photopolymerization, not affected by oxygen. The results were positive, with a substantial decrease in the photocrosslinking time and subsequent improvement in the shape fidelity. When washed and kept in water, these hydrogels showed signs of wear, which showed us this formulation did not lead to stable hydrogels.

The bioink that featured 3% (w/w) ChMA with 2% (w/w) CNC was tested in this new approach. A reduction in the amount of DTT was necessary due to the increased light sensitivity of this bioink, which prevented 3D bioprinting. This heightened sensitivity resulted from the higher concentration of photosensitive groups within this formulation. Very positive results were obtained, with decreased photocrosslinking time and better shape fidelity.

After all these tests, the best printing parameters were determined for this formulation and the frame design by observation and quantitative measurements, which were a printing flow of 100%, a printing velocity of 1 mm $s^{-1}$, 22 G nozzle, and a layer height of 0.2 mm. The obtained bioprinted structures evolved quite positively, leading to a structure with various similarities to the 3D model used. Quantitively, a decreased thickness and a larger width of the sides of the structure compared to the 3D model, coupled with the rounded pore, still verified a tendency of spreading of the filaments to the lower layers. Nonetheless, it's apparent that this tendency markedly decreased as the bioprinting process progressed, leading to a structure with good shape fidelity. For the grid design, however, the presented shape fidelity was lower, due to the higher complexity of the structure. This reveals the requirement of revaluation of the ideal printing parameters for this design.

Using these parameters and a formulation that included SPIONs it was not possible to obtain photocrosslinked structures due to the inability to crosslink this formulation, also observed in the production of hydrogels with moulds.

Hydrogels were produced using moulds with the best formulation for 3D bioprinting, to characterise the structures. Mechanical tests allowed the determination of the compressive modulus of the hydrogels, 70.82 ± 11.67 kPa, and assess their behaviour under compressive forces. PBS absorption tests permitted the determination of the higher PBS uptake of the hydrogels, 2493 ± 329 %, which occurred after 5 h. The verified instantaneous PBS absorption and stabilization afterwards are also worth mentioning. SEM images revealed the porous structure of the hydrogel, a positive feature for drug delivery applications, and the homogenous distribution of CNC on the structure. The images of the pore walls also revealed their layered structure.

## 4.2 Future Perspectives

The developments of this system in this work revealed its potential for 3D bioprinting and drug delivery applications. However, work towards the development of non-explored characteristics, assessment of the real applicability of the hydrogels and characterisation of this new system remains undone.

The exploration of SPIONs incorporation in the hydrogel must be conducted, since the first attempt at including them in the matrix did not allow photocrosslinking. The effect of SPIONs concentrations on the hydrogel and on the photocrosslinking process must be studied. The inclusion of coated SPIONs could also be an interesting approach. The success of SPIONs incorporation in the hydrogel could open the door to magnetic hyperthermia applications, which would be an asset in the treatment of cancer.

A deeper study of the effects of DTT concentration on the photocrosslinking time of the hydrogels would also be interesting since this compound is the key to the further improvement of the shape fidelity of these structures. 3D bioprinted structures with satisfactory shape fidelity including this component were successfully produced. However, further enhancements could be achieved through a study to determine the optimal concentration of this component in the hydrogel, that permits the shortest photocrosslinking time possible while preventing nozzle clogging, thus offering potential for further improvements.

The characterisation of this system must be developed as well. The nuclear magnetic resonance ($^1$H-NMR) in the characterisation of ChMA is required to confirm the methacrylation process and determine the degree of methacrylation of the polymer. This is essential for drawing conclusions regarding the efficacy of the methacrylation process, which correlates with the difficulties observed in dissolving the polymer in a neutral environment. The characterisation of more developed formulations must be performed as well, to assess the effect of each component on the characteristics of the hydrogel. Additionally, the characterisation of 3D bioprinted structures is necessary to evaluate the effect of the 3D bioprinting process on the hydrogel's characteristics.

Drug release tests would also be interesting to evaluate the applicability of these hydrogels in drug delivery. Finally, the study of the hydrogels' cytotoxicity must be performed to assess the possibility of their application in the biomedical field.

By combining the results achieved in this work with the aforementioned steps, the future of this technology appears optimistic and full of potential for developing innovative, customized and multifunctional drug delivery systems.

# BIBLIOGRAFIA


[1] "Cancer." Accessed: Mar. 28, 2024. [Online]. Available: https://www.who.int/health-topics/cancer#tab=tab_1

[2] "Cancer Today." Accessed: Mar. 28, 2024. [Online]. Available: https://gco.iarc.who.int/today/en/dataviz/tables?mode=population&group_populations=0&multiple_populations=1&types=0

[3] "Cancer Tomorrow." Accessed: Mar. 28, 2024. [Online]. Available: https://gco.iarc.who.int/tomorrow/en/dataviz/tables?types=0&populations=903_904_905_908_909_935_900

[4] H. Sung *et al.*, "Global Cancer Statistics 2020: GLOBOCAN Estimates of Incidence and Mortality Worldwide for 36 Cancers in 185 Countries," *CA Cancer J Clin*, vol. 71, no. 3, pp. 209–249, May 2021, doi: 10.3322/caac.21660.

[5] S. V. S. Deo, J. Sharma, and S. Kumar, "GLOBOCAN 2020 Report on Global Cancer Burden: Challenges and Opportunities for Surgical Oncologists," *Ann Surg Oncol*, 2022, doi: 10.1245/s10434-022-12151-6.

[6] F. Abasalizadeh *et al.*, "Alginate-based hydrogels as drug delivery vehicles in cancer treatment and their applications in wound dressing and 3D bioprinting," *Journal of Biological Engineering*, vol. 14, no. 1. BioMed Central Ltd, Mar. 13, 2020. doi: 10.1186/s13036-020-0227-7.

[7] K. McNamara and S. A. M. Tofail, "Nanoparticles in biomedical applications," *Advances in Physics: X*, vol. 2, no. 1. Taylor and Francis Ltd., pp. 54–88, 2017. doi: 10.1080/23746149.2016.1254570.

[8] D. Y. Fan, Y. Tian, and Z. J. Liu, "Injectable Hydrogels for Localized Cancer Therapy," *Frontiers in Chemistry*, vol. 7. Frontiers Media S.A., Oct. 11, 2019. doi: 10.3389/fchem.2019.00675.

[9] R. Narayanaswamy and V. P. Torchilin, "Hydrogels and their applications in targeted drug delivery," *Molecules*, vol. 24, no. 3. MDPI AG, Feb. 08, 2019. doi: 10.3390/molecules24030603.

[10] S. Yue, H. He, B. Li, and T. Hou, "Hydrogel as a biomaterial for bone tissue engineering: A review," *Nanomaterials*, vol. 10, no. 8. MDPI AG, pp. 1–25, Aug. 01, 2020. doi: 10.3390/nano10081511.

[11] A. Mellati, E. Hasanzadeh, M. Gholipourmalekabadi, and S. E. Enderami, "Injectable nanocomposite hydrogels as an emerging platform for biomedical applications: A review," *Materials Science and Engineering C*, vol. 131. Elsevier Ltd, Dec. 01, 2021. doi: 10.1016/j.msec.2021.112489.

[12] S. Beg *et al.*, "3D printing for drug delivery and biomedical applications," *Drug Discovery Today*, vol. 25, no. 9. Elsevier Ltd, pp. 1668–1681, Sep. 01, 2020. doi: 10.1016/j.drudis.2020.07.007.

[13] S. A. Meenach, C. G. Otu, K. W. Anderson, and J. Z. Hilt, "Controlled synergistic delivery of paclitaxel and heat from poly(β-amino ester)/iron oxide-based hydrogel nanocomposites," *Int J Pharm*, vol. 427, no. 2, pp. 177–184, May 2012, doi: 10.1016/j.ijpharm.2012.01.052.

[14] T. Vangijzegem *et al.*, "Superparamagnetic Iron Oxide Nanoparticles (SPION): From Fundamentals to State-of-the-Art Innovative Applications for Cancer Therapy," *Pharmaceutics*, vol. 15, no. 1. MDPI, Jan. 01, 2023. doi: 10.3390/pharmaceutics15010236.

[15] W. Hu, Z. Wang, Y. Xiao, S. Zhang, and J. Wang, "Advances in crosslinking strategies of biomedical hydrogels," *Biomaterials Science*, vol. 7, no. 3. Royal Society of Chemistry, pp. 843–855, Mar. 01, 2019. doi: 10.1039/c8bm01246f.

[16] X. Xue, Y. Hu, S. Wang, X. Chen, Y. Jiang, and J. Su, "Fabrication of physical and chemical crosslinked hydrogels for bone tissue engineering," *Bioactive Materials*, vol. 12. KeAi Communications Co., pp. 327–339, Jun. 01, 2022. doi: 10.1016/j.bioactmat.2021.10.029.

[17] V. P. Santos, N. S. S. Marques, P. C. S. V. Maia, M. A. B. de Lima, L. de O. Franco, and G. M. de Campos-Takaki, "Seafood waste as attractive source of chitin and chitosan production and their applications," *International Journal of Molecular Sciences*, vol. 21, no. 12. MDPI AG, pp. 1–17, Jun. 02, 2020. doi: 10.3390/ijms21124290.

[18] M. Zanon *et al.*, "Microwave-assisted methacrylation of chitosan for 3D printable hydrogels in tissue engineering," *Mater Adv*, vol. 3, no. 1, pp. 514–525, Jan. 2022, doi: 10.1039/d1ma00765c.

[19] M. Rajabi, M. McConnell, J. Cabral, and M. A. Ali, "Chitosan hydrogels in 3D printing for biomedical applications," *Carbohydrate Polymers*, vol. 260. Elsevier Ltd, May 15, 2021. doi: 10.1016/j.carbpol.2021.117768.

[20] S. Maiz-Fernández, L. Pérez-Álvarez, U. Silván, J. L. Vilas-Vilela, and S. Lanceros-Mendez, "Photocrosslinkable and self-healable hydrogels of chitosan and hyaluronic acid," *Int J Biol Macromol*, vol. 216, pp. 291–302, Sep. 2022, doi: 10.1016/j.ijbiomac.2022.07.004.

[21] U. Bozuyuk, O. Yasa, I. C. Yasa, H. Ceylan, S. Kizilel, and M. Sitti, "Light-Triggered Drug Release from 3D-Printed Magnetic Chitosan Microswimmers," *ACS Nano*, vol. 12, no. 9, pp. 9617–9625, Sep. 2018, doi: 10.1021/acsnano.8b05997.

[22] S. M. Saraiva, S. P. Miguel, M. P. Ribeiro, P. Coutinho, and I. J. Correia, "Synthesis and characterization of a photocrosslinkable chitosan-gelatin hydrogel aimed for tissue regeneration," *RSC Adv*, vol. 5, no. 78, pp. 63478–63488, 2015, doi: 10.1039/c5ra10638a.

[23] L. Zhu and K. M. Bratlie, "pH sensitive methacrylated chitosan hydrogels with tunable physical and chemical properties," *Biochem Eng J*, vol. 132, pp. 38–46, Apr. 2018, doi: 10.1016/j.bej.2017.12.012.

[24] D. K. Patel, T. V. Patil, K. Ganguly, S. D. Dutta, and K. T. Lim, "Nanocellulose-assisted 3D-printable, transparent, bio-adhesive, conductive, and biocompatible hydrogels as sensors and moist electric generators," *Carbohydr Polym*, vol. 315, Sep. 2023, doi: 10.1016/j.carbpol.2023.120963.

[25] T. M. S. U. Gunathilake, Y. C. Ching, and C. H. Chuah, "Enhancement of curcumin bioavailability using nanocellulose reinforced chitosan hydrogel," *Polymers (Basel)*, vol. 9, no. 2, p. 64, 2017, doi: 10.3390/polym9020064.

[26] B. Thomas *et al.*, "Nanocellulose, a Versatile Green Platform: From Biosources to Materials and Their Applications," *Chemical Reviews*, vol. 118, no. 24. American Chemical Society, pp. 11575–11625, Dec. 26, 2018. doi: 10.1021/acs.chemrev.7b00627.

[27] D. K. Patel, S. D. Dutta, K. Ganguly, and K. T. Lim, "Multifunctional bioactive chitosan/cellulose nanocrystal scaffolds eradicate bacterial growth and sustain drug delivery," *Int J Biol Macromol*, vol. 170, pp. 178–188, Feb. 2021, doi: 10.1016/j.ijbiomac.2020.12.145.

[28] H. Mao, C. Wei, Y. Gong, S. Wang, and W. Ding, "Mechanical and water-resistant properties of eco-friendly chitosan membrane reinforced with cellulose nanocrystals," *Polymers (Basel)*, vol. 11, no. 1, Jan. 2019, doi: 10.3390/polym11010166.

[29] P. Soares, "Chitosan-based magnetic nanoparticles for osteosarcoma theranostics," PhD thesis, Universidade Nova de Lisboa, Monte da Caparica, 2015.

[30] S. Fiejdasz, A. Gilarska, T. Straczek, M. Nowakowska, and C. Kapusta, "Magnetic properties of collagen–chitosan hybrid materials with immobilized superparamagnetic iron oxide nanoparticles (Spions)," *Materials*, vol. 14, no. 24, Dec. 2021, doi: 10.3390/ma14247652.

[31] K. Markstedt, A. Mantas, I. Tournier, H. Martínez Ávila, D. Hägg, and P. Gatenholm, "3D bioprinting human chondrocytes with nanocellulose-alginate bioink for cartilage tissue engineering applications," *Biomacromolecules*, vol. 16, no. 5, pp. 1489–1496, May 2015, doi: 10.1021/acs.biomac.5b00188.

[32] T. T. Demirtaş, G. Irmak, and M. Gümüşderelioğlu, "A bioprintable form of chitosan hydrogel for bone tissue engineering," *Biofabrication*, vol. 9, no. 3, Jul. 2017, doi: 10.1088/1758-5090/aa7b1d.

[33] Z. Gu, J. Fu, H. Lin, and Y. He, "Development of 3D bioprinting: From printing methods to biomedical applications," *Asian Journal of Pharmaceutical Sciences*, vol.

15, no. 5. Shenyang Pharmaceutical University, pp. 529–557, Sep. 01, 2020. doi: 10.1016/j.ajps.2019.11.003.

[34] A. Schwab, R. Levato, M. D'Este, S. Piluso, D. Eglin, and J. Malda, "Printability and Shape Fidelity of Bioinks in 3D Bioprinting," *Chemical Reviews*, vol. 120, no. 19. American Chemical Society, pp. 11028–11055, Oct. 14, 2020. doi: 10.1021/acs.chemrev.0c00084.

[35] G. Choi and H. J. Cha, "Recent advances in the development of nature-derived photocrosslinkable biomaterials for 3D printing in tissue engineering," *Biomaterials Research*, vol. 23, no. 1. BioMed Central Ltd., Nov. 19, 2019. doi: 10.1186/s40824-019-0168-8.

[36] N. S. Sumitha, S. Sreeja, P. J. G. Varghese, and G. S. Sailaja, "A dual functional superparamagnetic system with pH-dependent drug release and hyperthermia potential for chemotherapeutic applications," *Mater Chem Phys*, vol. 273, Nov. 2021, doi: 10.1016/j.matchemphys.2021.125108.

[37] P. Maturavongsadit, L. K. Narayanan, P. Chansoria, R. Shirwaiker, and S. R. Benhabbour, "Cell-Laden Nanocellulose/Chitosan-Based Bioinks for 3D Bioprinting and Enhanced Osteogenic Cell Differentiation," *ACS Appl Bio Mater*, vol. 4, no. 3, pp. 2342–2353, Mar. 2021, doi: 10.1021/acsabm.0c01108.

[38] Y. Shen *et al.*, "DLP printing photocurable chitosan to build bio-constructs for tissue engineering," *Carbohydr Polym*, vol. 235, May 2020, doi: 10.1016/j.carbpol.2020.115970.

[39] A. R. Osi *et al.*, "Three-Dimensional-Printable Thermo/Photo-Cross-Linked Methacrylated Chitosan-Gelatin Hydrogel Composites for Tissue Engineering," *ACS Appl Mater Interfaces*, vol. 13, no. 19, pp. 22902–22913, May 2021, doi: 10.1021/acsami.1c01321.

[40] C. Tonda-Turo *et al.*, "Photocurable chitosan as bioink for cellularized therapies towards personalized scaffold architecture," *Bioprinting*, vol. 18, Jun. 2020, doi: 10.1016/j.bprint.2020.e00082.

[41] E. S. Ko, C. Kim, Y. Choi, and K. Y. Lee, "3D printing of self-healing ferrogel prepared from glycol chitosan, oxidized hyaluronate, and iron oxide nanoparticles," *Carbohydr Polym*, vol. 245, Oct. 2020, doi: 10.1016/j.carbpol.2020.116496.

[42] D. Lin *et al.*, "Stabilizing Aqueous Three-Dimensional Printed Constructs Using Chitosan-Cellulose Nanocrystal Assemblies," *ACS Appl Mater Interfaces*, vol. 12, no. 49, pp. 55426–55433, Dec. 2020, doi: 10.1021/acsami.0c16602.

[43] S. Sayyar, S. Gambhir, J. Chung, D. L. Officer, and G. G. Wallace, "3D printable conducting hydrogels containing chemically converted graphene," *Nanoscale*, vol. 9, no. 5, pp. 2038–2050, Feb. 2017, doi: 10.1039/c6nr07516a.

[44] S. Samani, S. Bonakdar, A. Farzin, J. Hadjati, and M. Azami, "A facile way to synthesize a photocrosslinkable methacrylated chitosan hydrogel for biomedical applications," *International Journal of Polymeric Materials and Polymeric Biomaterials*, vol. 70, no. 10, pp. 730–741, 2021, doi: 10.1080/00914037.2020.1760274.

[45] A. Tagaya, H. Ohkita, M. Mukoh, R. Sakaguchi, and Y. Koike, "Compensation of the Birefringence of a Polymer by a Birefringent Crystal." [Online]. Available: www.sciencemag.org

[46] D. F. T. Silva, A. S. L. Gomes, B. De Campos Vidal, and M. S. Ribeiro, "Birefringence and second harmonic generation on tendon collagen following red linearly polarized laser irradiation," *Ann Biomed Eng*, vol. 41, no. 4, pp. 752–762, Apr. 2013, doi: 10.1007/s10439-012-0720-3.

[47] H. Yang, S. Chen, L. Liu, C. Lai, and X. Shi, "Synthesis, characterization and osteogenesis of phosphorylated methacrylamide chitosan hydrogels," *RSC Adv*, vol. 8, no. 63, pp. 36331–36337, 2018, doi: 10.1039/c8ra05378b.

[48] N. B. Milosavljević, N. Z. Milašinović, I. G. Popović, J. M. Filipović, and M. T. Kalagasidis Krušić, "Preparation and characterization of pH-sensitive hydrogels based on chitosan, itaconic acid and methacrylic acid," *Polym Int*, vol. 60, no. 3, pp. 443–452, Mar. 2011, doi: 10.1002/pi.2967.

[49] N. Cankaya, "Grafting of Chitosan: Structural, Thermal and Antimicrobial Properties," 2019.

[50] C. F. C. João, C. Echeverria, A. Velhinho, J. C. Silva, M. H. Godinho, and J. P. Borges, "Bio-inspired production of chitosan/chitin films from liquid crystalline suspensions," *Carbohydr Polym*, vol. 155, pp. 372–381, Jan. 2017, doi: 10.1016/j.carbpol.2016.08.039.

[51] K. H. Kang, L. A. Hockaday, and J. T. Butcher, "Quantitative optimization of solid freeform deposition of aqueous hydrogels," *Biofabrication*, vol. 5, no. 3, Sep. 2013, doi: 10.1088/1758-5082/5/3/035001.

[52] B. Webb and B. J. Doyle, "Parameter optimization for 3D bioprinting of hydrogels," *Bioprinting*, vol. 8, pp. 8–12, Dec. 2017, doi: 10.1016/j.bprint.2017.09.001.

[53] J. Kim, J. Oh, W. K. Hyun, M. D. Feldman, and T. E. Milner, "Photothermal response of superparamagnetic iron oxide nanoparticles," *Lasers Surg Med*, vol. 40, no. 6, pp. 415–421, Aug. 2008, doi: 10.1002/lsm.20650.

[54] S. Del Rosso and L. Iannucci, "On the compressive response of polymeric cellular materials," *Materials*, vol. 13, no. 2, Jan. 2020, doi: 10.3390/ma13020457.

[55] M. Di Giuseppe *et al.*, "Mechanical behaviour of alginate-gelatin hydrogels for 3D bioprinting," *J Mech Behav Biomed Mater*, vol. 79, pp. 150–157, Mar. 2018, doi: 10.1016/j.jmbbm.2017.12.018.

[56] B. Melo, "Chitin nanocrystals-alginate bioinks for bioprinting of 3D structures," MSc thesis, Universidade Nova de Lisboa, Monte da Caparica, 2019.

# A

# ANNEXES

## A.1 Characterisation methods

Fourier-transformed infrared (FTIR-ATR) was obtained through an attenuated total reflectance (ATR) sampling accessory (Smart iTR) featuring a single bounce diamond crystal on a Thermo Nicolet 6700 spectrometer. The data was recorded at room temperature, in the range of 500 $cm^{-1}$ to 4000 $cm^{-1}$, with 45º of incident angle and 4 $cm^{-1}$ resolution. Regarding scanning calorimetry with thermogravimetric analysis (DSC-TG), the analysis was performed using a Netzsch 449 F3 Jupiter® simultaneous thermal analyzer. The samples were heated until 550 ºC, with increments of 10 ºC $min^{-1}$, in an inert atmosphere.

Rheologic characterisation was performed using a Anton Par MCR 502 rotational rheometer at 25 ºC. A plate-plate geometry was used, with 25 mm of diameter and 1 mm gap size. The shear rate was increased from 0.1 $s^{-1}$ to 100 $s^{-1}$.

For PBS absorption tests, 7 samples were freeze-dried and immersed in phosphate-buffered saline (PBS) for 5 min, 10 min, 20 min, 30 min, 1 h, 2 h, 3 h, 4 h and 5 h. The PBS was prepared following standard protocols and had a pH of 7.4. The hydrogel mass was registered after removing the PBS excess, and the PBS was changed between measurements. The mechanical tests were performed in a Rheometric Scientific uniaxial machine operated with Minimat software in compression mode. The maximum load was 19 N and the measurements were performed at room temperature.

Scanning electron microscopy (SEM) analysis was conducted using a Hitachi Regulus SU8220. The hydrogel underwent freeze-drying, followed by immersion in liquid nitrogen at -196 ºC and sectioned using a bistoury, enabling observation of the cross-sectional area. Subsequently, a 15 nm gold layer was deposited onto the samples using a Q150T ES Quorum Sputter Coater. This process enabled the acquisition of both cross-sectional and top-view images of the samples.

## A.2 Fourier-Transformed Infrared with Attenuated Total Reflectance (FTIR-ATR)

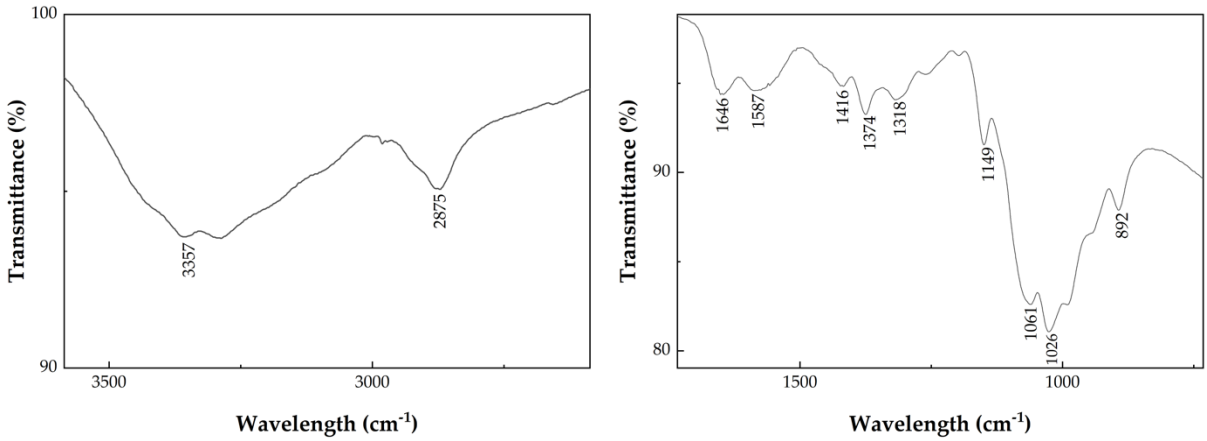


Figure 4-1 - FTIR-ATR of chitosan, divided into two zoomed-in images.

## A.3 3D printing

The bioprinted designs were modeled at software Blender and are presented in Figure 4-2. Both designs have 10x10x1.638 mm in terms of length, width, and thickness.

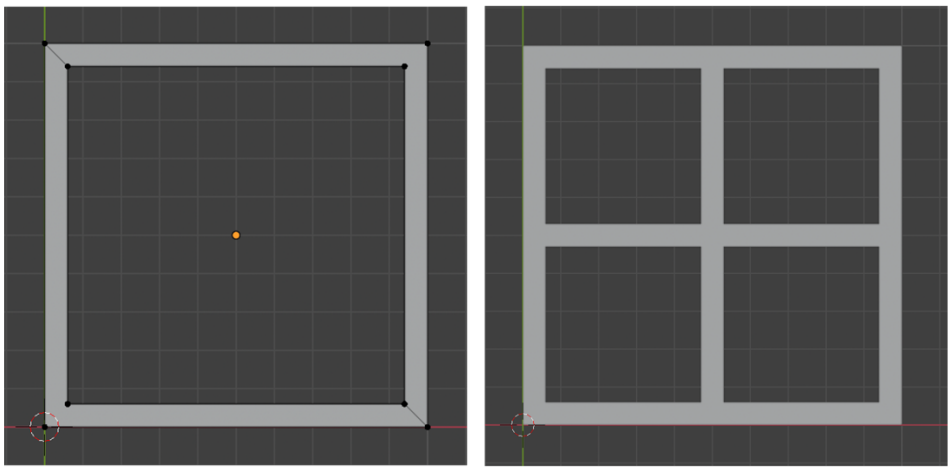

Figure 4-2 – 3D models used in the 3D printer software to obtain the bioprinted hydrogels. Grid: 1 mm.